UNIVERSITY OF COPENHAGEN
FACULTY OF SCIENCE

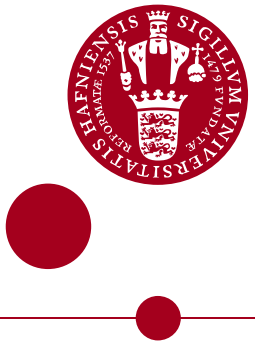

Master Thesis

Impact of snow albedo parameterization over the Greenland ice sheet on the simulated climate of EC-Earth3

Dana Lüdemann

Advisors: Eigil Kaas, Marianne Sloth Madsen, Shuting Yang

Submitted: 31.05.2022

Thesis project in collaboration between NBI and DMI.

Abstract

The albedo of snow and ice has a strong positive feedback loop that controls the amount of solar radiation absorbed by the surface. Snow melt induced by surface warming will lead to a decreased albedo that allows for more solar radiation to reach the surface and will further increase the melting and surface warming. In current climate models, the albedo over perennial snow is kept constant and thus, can not represent this feedback. In the recent past, a more realistic snow albedo parameterization has been incorporated into the global climate model EC-Earth3 over the Greenland ice sheet. To analyze and understand the impact of this new parameterization, three experiments were performed using the atmospheric general circulation model (A-EC-Earth3). Each experiment - (1) a control experiment, (2) an experiment using new albedo scheme and (3) an extreme experiment with a low albedo of 0.6 over perennial snow, contains three members which only differ in their initial state. Locally, the new albedo parameterization introduces a seasonal cycle of albedo over Greenland and Ellesmere Island, with an overall decreased snow albedo compared to the control simulations. The new albedo scheme is responsive to changes in temperature and precipitation, which results in local reductions of the temperature biases of EC-Earth3. However, the albedo scheme shows deficits in the snow albedo estimation over the Greenland ice sheet. The local changes in surface energy fluxes suggest that the lowered albedo leads to a larger uptake of energy by the surface, while highlighting that the applied albedo forcing is small. The remote response in near surface temperature, mean sea level pressure and 500 hPa geopotential height shows no systematic pattern. Moreover, only two out of three ensemble members show a significant response to the albedo forcing. The found anomalies can be explained by the large internal variability of the atmosphere, raising awareness to its role when investigation atmospheric responses to forcings.

Preface

This master project was carried out in collaboration between the Danish Meteorological Institute (DMI) and The University of Copenhagen, Niels Bohr institute (NBI). The following thesis report was submitted for the degree of Master of Science in *Physics, Computational Physics* at The University of Copenhagen, NBI in May 2022.

Course: Degree Project in Physics, **45 ECTS** (NFYK10021E)

University Supervisor: Eigil Kaas
External Supervisors: Marianne Sloth Madsen, Shuting Yang
Censor: Peter Aakjaer

Acknowledgements

I would like to express my gratitude towards my supervisors Shuting Yang, Marianne Sloth Madsen and Eigil Kaas for their guidance and support in this thesis project. Even in these strained times with plenty of restrictions, they always were happy to give me encouraging words and insights throughout the entity of the project.

I would especially like to thank Peter Thejl for guiding me through all the statistics question and having an open ear for me.

A huge thanks goes to my friend Nga Ying Lo, who sat with me during the whole project and kept my spirits high. I am beyond glad to have you as my mental support and friend.

Lastly, I would like express my love and appreciation for my family and friends. Their emotional support and relentless source of motivation have been of immense value to me.

Contents

List of Abbreviations

AMIP	Atmospheric Model Intercomparison Project
AO	Arctic Oscillation
BC	Black Carbon
CDO	Climate Data Operator
ECMWF	European Centre of Medium Range Weather Forecast
ESM	Earth System Model
GCA	General Circulation of the Atmosphere
GCM	Global Climate Model
GPH	Geopotential Height
GrIS	Greenland ice sheet
HTESSEL	Hydrology Tiled ECMWF Scheme of Surface Exchanges over Land
IFS	Integrated Forecasting System
IPCC	Intergovernmental Panel on Climate Change
ITCZ	Intertropical Convergence Zone
K-S	Kolomogorov-Smirnov
LAP	Light Absorbing Particles
LGM	Last Glacial Maximum
LW	Long Wave
MMC	Mean Meridional Circulation
MODIS	Moderate Resolution Imaging Spectroradiometer
MSL	Mean Sea Level pressure
NAM	Northern Annular Mode
NWP	Numerical Weather Prediction
NH	Northern Hemisphere
OLR	Outgoing Longwave Radiation
PBL	Planetary Boundary Layer
RCM	Regional Climate Model
RH	Relative Humidity
SAF	Snow Albedo Feedback
SH	Southern Hemisphere
SMB	Surface Mass Balance
SSHF	Surface Sensible Heat Flux
SSLF	Surface Latent Heat Flux
SSR	Surface Solar Radiation
SST	Sea Surface Temperature
STR	Surface Thermal Radiation
SW	Short wave
T2M	Two Meter Temperature
TOA	Top of the Atmosphere

Chapter 1

Introduction

Snow covered surfaces play a crucial role in Earth's climate system. Their impact can be felt locally through modulating the energy balance by reflecting solar radiation, as well as globally by coupling to the atmosphere and its general circulation. Several factors contribute to their climatic impact, such as the thermal emissivity of snow, its insulating properties and most importantly the high surface albedo of snow.

The snow albedo has a positive, radiative feedback meaning that snow melt induced by a surface warming will decrease the albedo. This decrease allows for more solar radiation to reach the surface and further increase melting and warming. The snow albedo feedback (SAF) has long been known to enhance the climate sensitivity at high latitudes as shown by studies from Budyko (1969) and North (1975). Their simple energy balance models demonstrated the strong positive feedback between Arctic temperature perturbations and ice and snow, thereby laying the ground work for understanding the SAF. One of the first correlations between snow cover extent and global warming was derived by Groisman et al. (1994), showing that the SAF forcing is largest during northern hemisphere spring time.

On a global scale, the SAF attributes to a forcing of $\sim 0.04 \pm 0.02$ W/m^{2}C$^\circ$ (Xiao et al., 2017) being only a small fraction of radiative forcing exerted by water vapour. However on hemispheric scales the SAF amounts to $\sim 0.18 \pm 0.08$ W/m^{2}C$^\circ$ and drives the regional climate of the NH. The strongest SAF on the NH is located north of 30°N and exerts 1 % decrease in surface albedo per degree of warming during springtime (Thackeray and Fletcher, 2016).

With Arctic temperatures rising twice as fast as the global average (Meredith et al., 2019), snow albedo exerts a substantial forcing on the cryosphere. Even though the drivers of the Arctic amplification are still debated, the latest climate report AR6

(IPCC, 2021) identifies the snow and ice albedo as one of the main contributors. For example, the increasing mass loss of the Greenland ice sheet (GrIS) is strongly enhanced by the SAF and the resulting contributions to sea level rise will be felt globally.

For accurate future climate projections, global climate models (GCMs) need to resolve a manifold of processes, among other things the ice sheets and their exchanges with the climate system. In an recent effort to improve the surface mass balance of the GrIS, a new snow albedo parameterization over perennial snow was implemented into the Earth System Model EC-Earth3 (Döscher et al., 2022). The snow albedo in the standard set-up was kept constant over ice sheets, failing too represent a realistic surface albedo and SAF over the GrIS. Parts of the local impact of this new parameterization were thoroughly discussed in studies by Helsen et al. (2017). The results show local improvements over the GrIS, but lack an investigation of its remote impact.

This thesis is an investigation to understand and quantify the impact of this new parameterization on the simulated climate of EC-Earth3 and thereby, the general circulation of the atmosphere. The questions this thesis will answer are:

- What is the impact of a better representation of snow albedo over Greenland to the atmospheric circulation in present day climate?
- Can the new snow albedo parameterization reduce the model biases, in particular in regions remote to Greenland?
- What circulation changes are related to the update of the snow albedo parameterization?

In this study, three atmosphere only experiments were conducted: a control experiment with the standard albedo scheme, an experiment with the new albedo parameterization and an extreme experiment with a constant low albedo over ice sheets. Each experiment contains three simulations (members), which differ only in their initial state. The experiments will be compared and the observed changes will be tested on their statistical significance. The following section will give an overview of the thesis structure.

1.1 Overview

The section 2 describes the background for the thesis, covering the theory and the literature review. The background is divided into three subjects: Earth's energy budget, albedo and the general circulation of the atmosphere. This covers the main topics needed to understand the climatic response of the albedo forcing.

The section 3 presents the EC-Earth3 model. It contains a detailed description of the land surface model HTESSEL and how the snow albedo is parameterized, i.e., explaining the standard and new albedo scheme. Further, the experimental set-up is covered in this section, showing all the runs and their different configurations.

In section 4 the data handling is explained by first visiting the theory behind the statistical tests and then comparing the methods against each other. The better suited test is used to analyze the data.

The results and discussion are divided into two sections: the local impact in section 5 and the remote impact in section 6. In the local section, observed differences close to the Greenland ice sheet are discussed, i.e., radiative fluxes and albedo changes. The division was made to highlight difference in local and remote responses. The remote impacts discuss different climate variables such as two meter temperature, mean sea level pressure and geopotential height.

Section 7 summarizes the main findings of this thesis and highlights improvements for future work.

Chapter 2

Background

Incoming solar radiation is the primary driver of Earth's climate system and a central component of Earth's energy budget. The absorption of this short-wave radiation is governed by the albedo. In general, Earth's changing energy budget is in approximate balance, meaning that the energy received by the sun is released back into space. However, perturbations to this balance lead to climate changes such as increasing global surface temperature or sea level rise. A direct measure for these perturbations exerted by different climate components is radiative forcing (in units W/m^2), which scientists try to qualify and quantify in order to understand global climate changes. The coming section will discuss the theory and background behind Earth's energy budget in 2.1, and albedo with a special focus on the snow albedo and its feedback processes in 2.2. Since this thesis uses a general circulation model to simulate the climate, the general circulation of the atmosphere is discussed in 2.3. The first two sections will follow an unpublished literature project written by the author (Lüdemann, 2021).

2.1 Earth's energy budget

Earth's energy budget describes the balance between the amount of incoming solar radiation and the amount of energy that Earth radiates back into space in the form of reflected sunlight and thermal radiation. Moreover, it accounts for how energy moves throughout the climate system. Almost all of the incoming energy is matched, making the energy budget a close balance. Figure 2.1 depicts the energy budget and all its components, including the remainder of the balance. This remainder, accumulated as global warming, has grown over the past years (2011-2018) from 0.6 to 0.79 W/m^2, as reported in the AR6 (IPCC, 2021). Global temperature rise is a restoring response to a shift in the budget, which occurs delayed due to the thermal inertia of oceans, land and cryosphere.

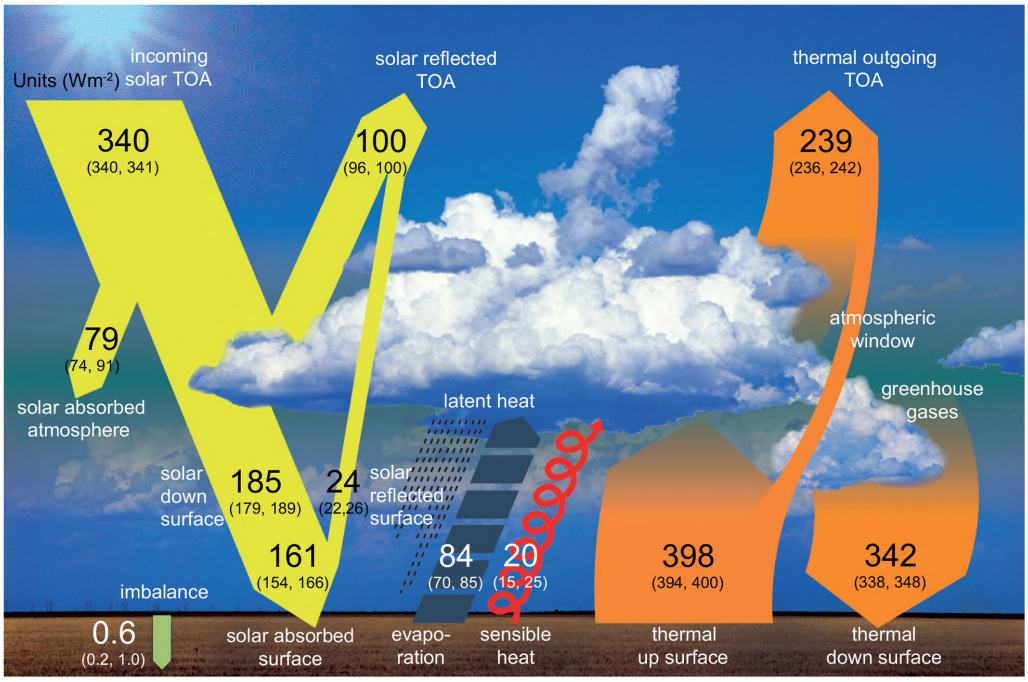

Figure 2.1: Global mean energy budget under present-day climate conditions. Reprinted with permissions from AR5 (Hartmann et al., 2013).

Essentially, Earth receives all its energy from the sun, amounting to 340 W/m^2, of which 29% is reflected due to clouds, dust, snow, and Earth's surface, known as the planetary albedo. From figure 2.1, it is visible that the atmospheric contribution to the planetary albedo (reflecting about ∼76 W/m^2) is larger than the surface contribution (reflecting ∼24 W/m^2). During past ice ages, the surface albedo was more important to the energy budget, which will be highlighted in section 2.2.4

Of the remaining 240 W/m^2, a quarter is absorbed by the atmosphere. The rest is transformed into thermal energy via the surface. The atmosphere absorbs a large part of the radiation and radiates it in both directions: into space and down to the Earth's surface. Actually, Earth's surface gets double the amount of radiation from the atmosphere than directly from the sun. Overall, the Earth emits about 79% percent of the energy received by the surface and the atmosphere. The remainder is released as sensible and latent heat.

2.2 Albedo

As described in the previous section, Earth's changing energy budget is in approximate balance. This means that the incoming solar radiation must either be reflected, transmitted or absorbed by the surface. The term albedo describes the fraction of sunlight a surface or material reflects, ranging between values of 0 and 1. The higher the albedo, the more sunlight is reflected by the surface; therefore, fresh snow exerts a surface cooling by reflecting about 90% of the sunlight.

Surface	**Remarks**	**Albedo in %**
Clouds	thick	60 - 90
	thin	30 - 50
Forest		3 - 10
Fresh snow		75 - 90
Grassy field		10 - 30
Ice	sea	30 - 45
	glacier	20 - 40
Sand		15 - 45
Water	daily average	10

Table 2.1: Typical albedo values of different surface types. Values originate from Oke (1987); Ahrens and Henson (2017).

For example, a surface absorbing half of the incident sunlight would have an albedo of 50%, corresponding to a value of 0.5. In the visible spectrum, the albedo of an object can be determined by its brightness - white snow has a high albedo, while charcoal has a low albedo.

While incident sunlight travels through the atmosphere towards the surface, it can be reflected on many different atmospheric constituents such as clouds, aerosols and Green house gases, which all have their own radiative properties. Table 2.1 above shows typical albedo values from various surface types.

Even though the surface properties play a significant role in the average reflectance, it should be noted that the spectral and angular distribution of the sunlight itself has an impact too. Sunlight is defined as the entire frequency spectrum of electromagnetic radiation received from the sun. Therefore, we can infer a spectral albedo by only looking at specific wavelength intervals. However, without further specification, the albedo analyzed in this thesis is the broadband albedo which covers ultraviolet, visible and infrared radiation (Coakley, 2003).

In short, albedo does not only vary with surface type but also over time, geographical location (i.e., solar zenith angle) and atmospheric composition.

On a yearly average, Earth will reflect about 29 % of the incident solar radiation, which is known as the planetary albedo. However, regional impacts can be large, especially in the cryosphere, which includes all parts of Earth where frozen water is essential (e.g., the continental ice sheets Greenland and Antarctica).

2.2.1 Snow albedo

The amount of sunlight that can be reflected by snow is directly dependent on the snows condition, which is why the albedo of fresh snow can fall from 0.9 to 0.5 in just a matter of days (Wiscombe and Warren, 1980). The processes affecting snow albedo can be part of its composition as well as external factors, all leading to a decrease in albedo over time.

Two of the most important physical factors are snow grain morphology (size and shape) and impurity concentration. Starting from freshly precipitated snow, the snow grains or crystals change their shape over time, known as snow metamorphism. The grain size can change in dry conditions due to mass transfer from warmer to colder grains or under wet conditions due to large grain growth from adhesion of water to the ice crystals (Langlois et al., 2020). These wet conditions can be induced by an increase in snow temperature, which also leads to darkening of snow due to water having a lower albedo. An increasing grain size causes a decrease of scattering within the snow. The incident light has to travel further in coarse grains, decreasing the refraction events and the overall albedo. The largest effects of snow morphology are seen for albedo in the near-infrared spectrum (Aoki et al., 2003). In the visible spectrum, impurities such as black carbon (BC) and dust effectively lower the albedo by absorbing light (Wiscombe and Warren, 1980).

Snow thickness can also affect the snow albedo since the underlying surface is most likely less reflective. As the snow pack thickens, the impact of the surface below reduces. However, the thickness at which the surface albedo is not affected by its underlying surface is dependent on wavelength and snow properties. The external factors contributing to snow albedo changes include solar zenith angle and the ratio between diffuse and direct light conditions.

Specular reflection of the sun above the horizon affects the albedo, meaning that a high zenith angle will lead to a high albedo and vice versa. Further, snow is good at reflecting diffuse radiation - light which is scattered at all angles. At times of high cloud coverage, the albedo is high due to clouds scattering the light and snow reflecting the resulting diffuse light.

2.2.2 Ice albedo

With an albedo ranging from 0.5 to 0.7, ice is another surface with high reflectance. Especially sea ice is of immense importance to the climate system, as well as a good indicator of climatic changes. Likewise to the case of snow, the sea ice albedo is dependent on several processes such as ice thickness, the melt pond fraction, brine volume and air bubbles. Moreover, ice growth rate and melting conditions, and wavelength of the incoming solar radiation have an impact on its albedo (Køltzow, 2007).

2.2.3 Feedback processes in the cryosphere

Earth's energy balance can be perturbed by processes such as radiative climate feedbacks. These feedbacks can either be positive or negative, relating to and intensification or reduction on tendencies leading to climate change. However, to not get run-away tendencies, various positive and negative processes interplay in our Earth system. Figure 2.2 shows the radiative and non-radiative feedbacks in the cryosphere.

The most fundamental feedback is the Plank feedback, which prescribes the amount of outgoing longwave radiation (OLR) in relation to surface temperate. Due to colder surface temperatures, this feedback is less negative in the polar regions than in the tropics. The lapserate feedback in the Arctic is positive since stable stratification (atmosphere cooling less than 1°C per 100m) there inhibits vertical mixing and leads to near surface warming. The feedback is negative in the tropics and 0 in the antarctic (Goosse et al., 2018). The most important green house gas, water vapour, amplifies warming and the green house gas effect. This positive feedback is again strongest in the tropics but plays an essential role in the polar regions.

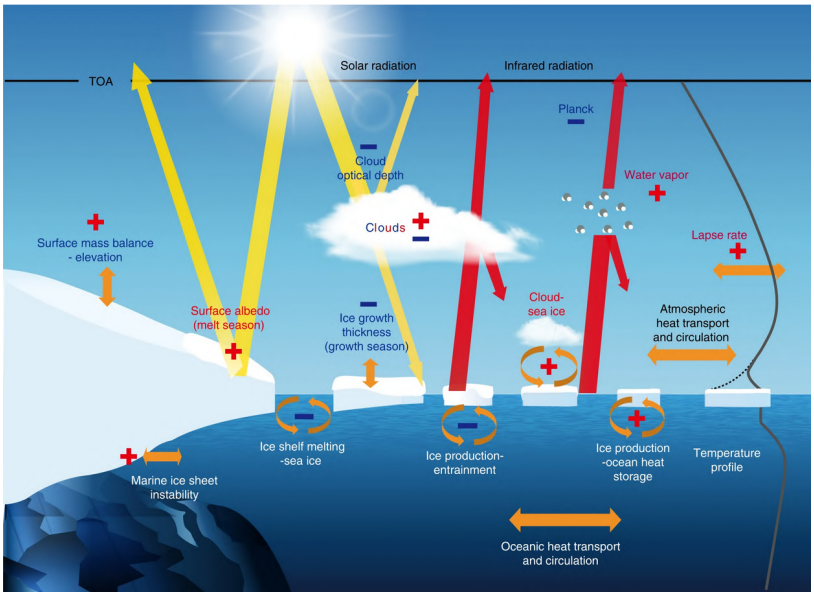

Figure 2.2: Schematic showing the radiative and non-radiative feedback processes in the cryosphere concerning the atmosphere, the ocean, sea ice and ice sheets. The feedback's nature can be either positive or negative in the polar region. The gray line at the right shows the mean temperature profile in the regions. Reprinted with permission from Goosse et al. (2018).

A key feedback in this thesis is the positive snow- or ice-albedo feedback. It could be set off by an increase in global surface air temperature, which causes melting of snow and ice in the polar regions. This melting would reduce the overall albedo in these latitudes allowing for more solar energy to be absorbed by the surface, which would further raise the air temperature. This feedback shows the strong coupling between the atmosphere and the cryosphere.

Additional feedbacks in the cryosphere are related to clouds. However, their feedback processes are most uncertain since many factors are involved.

2.2.4 Climate sensitivity due to snow & ice albedo

The coupling between cryosphere and atmosphere exerts substantial variations on the near surface temperature through the ice-albedo feedback. This feedback has an impact on the interannual variability, as well as on timescales ranging from intraseasonal to ice ages. On shorter timescales, such as centuries, snow and sea ice dominate the climate variability, while over millennia slowly evolving continental ice sheets are more important (Wallace and Hobbs, 2006).

With using a simple quantitative method to determine the cause of glaciations, Budyko could show that a change in radiation of 1.6% could lead to a full glacia-

tion of Earth (Budyko, 1969). This corresponds to a 0.02 unit change in planetary albedo and is strongly enhanced by the ice-albedo effect. Moreover, only using the ice-sheet albedo as feedback, North showed that a 7% decrease in albedo would be required for ice age instability (North, 1975). A change in planetary albedo of 0.01 is estimated to have a similar global mean warming effect as doubling the amount of Carbon dioxide above the preindustrial atmospheric concentration (IPCC, 2021). All this highlights the importance of albedo on the climate system and gives reason to study what changes the albedo and drives these perturbations.

The planetary albedo is a function of climate state and relies on the optical properties of atmospheric constituents (e.g., clouds, water vapor, and aerosols) and surface constituents (e.g., ice, ocean, and trees) (Hall, 2004), see figure 2.3. Changes in surface albedo impact the planetary albedo; however it should be noted that the direct impact is lowered due to atmospheric absorption and scattering. This means that the atmosphere attenuates the effect surface contribution to the climatological planetary albedo (Qu and Hall, 2005). Moreover, surface albedo reductions due to the ice-albedo effect are weakened by cloud thickening in the Arctic and southern ocean (Block and Mauritsen, 2013).

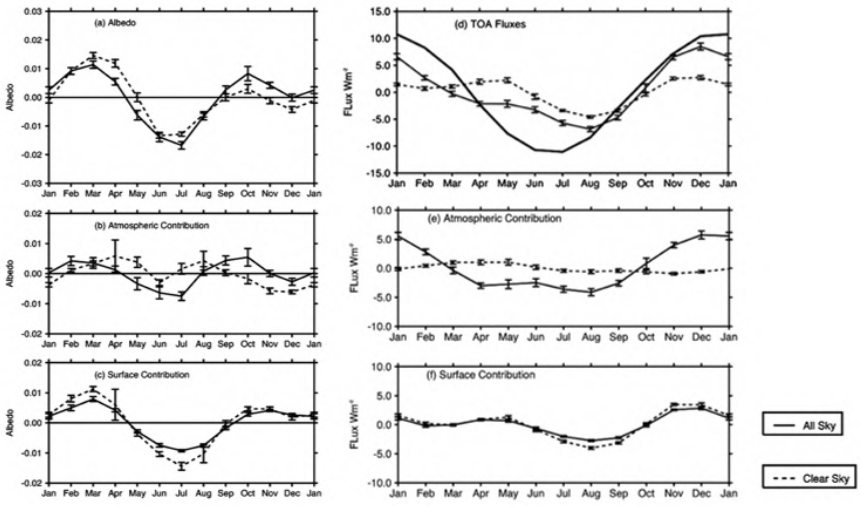

Figure 2.3: Seasonal cycles being an average of 13 annual cycles of CERES 2.7r data, broken down into its components for all-sky and clear-sky fluxes: (a) the globally averaged albedo, (b) the atmospheric and (c) surface contributions, (d–f) the respective cycles of the global mean fluxes. In 5d, the thick curve is the annual solar insolation, annual means have been subtracted and the error bars show the inter annual variability. Adapted with permission from Stephens et al. (2015).

In figure 2 the seasonal cycles of albedo and TOA fluxes are shown for clear-sky and all-sky conditions, underlining the dampening effect of clouds and atmospheric constituents. Although dampened, the surface contributions of the albedo dominates the variability in planetary albedo on seasonal and inter annual time scales (Qu and Hall, 2005), see sub figure 2a,2c.

The ice-albedo feedback has its largest importance during glacial intervals, which are characterized by colder, drier, dustier conditions and advanced glaciers. For the last glacial maximum (LGM), about 20.000 years ago, researchers estimated the planetary albedo to be of 1 percent higher than the current value of 0.29, showing the significance of the ice-albedo effect on the scale of ice ages. A radiative forcing of 3.9 W/m^2 (spread 2.7 to 5.2 W/m^2) was estimated for the impact of LGM ice sheets, using 11 climate models of intermediate complexity (Abe-Ouchi et al., 2015).

In 1987, Broccoli et al. identified amplified flow pattern and enhanced westerlies around the North American and Eurasian ice sheets during the LGM due to the ice-albedo effect (Broccoli and Manabe, 1987). The difference in radiative properties between snow-covered and snow-free surfaces creates a temperature gradient between the tropics and polar regions, driving our atmospheric circulation. A change in snow and ice extent can then lead to local temperature and circulation changes, which part of the regional impacts of the ice-albedo feedback.

The local changes include changes in the arctic surface air temperature. This has increased more than twice the global average over the last two decades driven by athropogenic green house gas forcing. Further, between 2011 and 2020 the annual average sea ice area is at its lowest since 1850, or maybe even further in the past (IPCC, 2021). Even though the arctic amplification mechanisms are still debated, a contributing factor is the reduced summer albedo due to sea ice and snow cover loss (Meredith et al., 2019).

The antarctic ocean changed from having a thick multiyear ice cover, to having larger seasonal ice zones characterised by thin, first- year ice. Melting the seasonal sea ice, decreases the surface albedo since the darker ocean can now absorb solar radiation. This is known as the ice-ocean albedo feedback, which occurs due to the contrast of ice and water, and increases summer sea ice retreat in areas of seasonal sea ice (e.g., Southern ocean) (Kashiwase et al., 2017). Using satellite and reanalysis data, Cao et al. (2015) assessed the radiative forcing of the sea ice albedo feedback to be 0.25 W/m^2K for the northern hemisphere and 0.19 W/m^2K for the entire globe.

The sea-ice albedo feedback is a key driver of sea ice loss, and worsened by the transition from perennial snow to seasonal sea ice. Parts of this transition can be accounted by darkening of snow through depositions of light absorbing particles (LAP),

like Black carbon (BC) or dust. BC is part of naturally and anthropogenic soot, produced through incomplete combustion of fossil fuels. These highly light absorbent particles can enter the atmosphere through various sources such as diesel engines, forest fires or cook stoves. The direct radiative forcing associated with black carbon in seasonal snow and over ice amounts to 0.04 W/m^2. However, on regional scales this effect can triple due to an enhanced ice-albedo effect set off by the darkening (Meredith et al., 2019).

Overall, Earth's climate system is sensitive to changes in snow and ice albedo raising the importance to further study and quantify its climatic impacts.

2.3 General circulation of the atmosphere

The difference between incident solar radiation (insolation) and outgoing terrestial radiation at the top of the atmosphere (TOA) gives the net radiation at the TOA. Averaged over the entire globe and annually, this net radiation shows the approximate balance of Earth's energy budget. However, observing the aspects of Earth's radiation budget averaged over latitudinal bands, so called zones, shows a radiative imbalance between the equatorial and polar regions (see fig. 2.4).

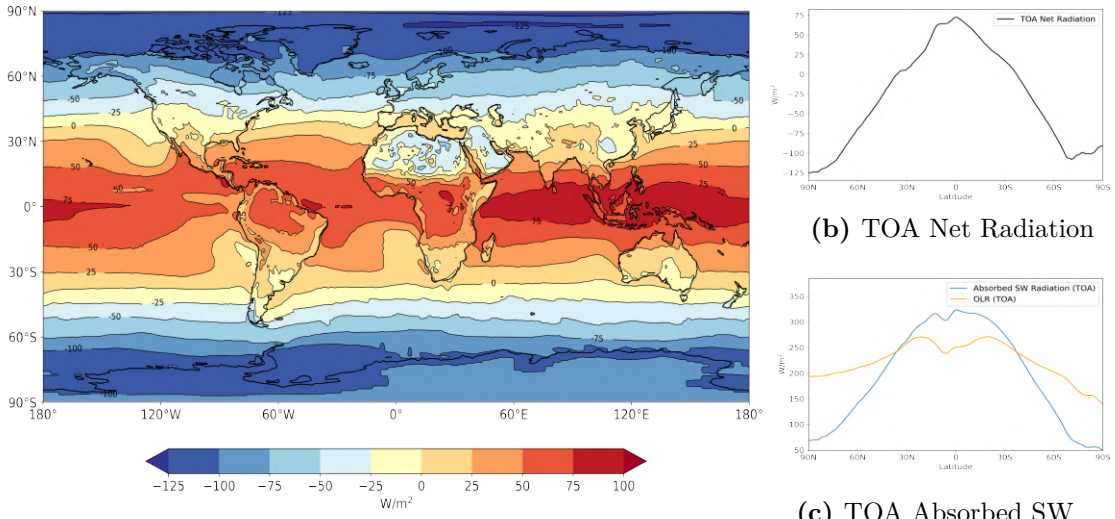

(a) TOA Net Radiation

(b) TOA Net Radiation

(c) TOA Absorbed SW & OLR

Figure 2.4: The net radiation at the top of the atmosphere (TOA) is shown in (a) and zonally averaged in (b). Its components, i.e. the outgoing longwave radiation (OLR) and absorbed shortwave (SW) radiation, are given zonally averaged in (c). The data shows the multiyear mean, between 2001-2015, of the satellite data product CERES EBAF ed. 4.0 (Loeb et al., 2018)

.

As a result of Earth's spherical shape, the insolation at the TOA is largest at the tropics and weakest at the poles. Earth's albedo increases towards the polar regions due to snow, ice and clouds, giving the absorbed shortwave (SW) radiation at the TOA a similar characteristic to the insolation (see fig. 2.4c). The outgoing longwave radiation (OLR) at the TOA also decreases towards the poles (see fig. 2.4c). The OLR has its maxima at the subtropics and a minima at the tropics, due to high clouds and water vapour entrapping the radiation, i.e. the Intertropical Convergence Zone, or ITCZ. In combination, the resulting net radiation at the TOA shows a surplus of energy in the tropics and a deficit of energy at the poles (see fig. 2.4b).

This imbalance is compensated through meridional energy transports by the atmosphere and the oceans in form of circulations. In this thesis the focus lies on observing responses in the simulated climate of EC-Earth3, which uses the atmospheric module as a stand alone. To understand the response and impact of the new albedo parameterization, it is essential to understand the main features of the general circulation of the atmosphere. The atmospheric circulation can be seen as circulating mass of "dry air" and three phases of water, which carry evolving energy and momentum along Randall (2015). The following will this discuss the main aspects of the GCA.

2.3.1 Atmospheric structure and boundary

The atmosphere can be divided meridionally (north-south direction), zonally (in latitude circles) and vertically (height above mean sea level z). To understand the aspects of the GCA, the vertical structure as well as the boundary should be visited.

Vertical structure

The lowest vertical layer, with an approximate depth of 1 km, is the planetary boundary layer, or PBL. The air in the PBL is turbulent, producing rapid moisture exchanges through evaporation (latent heat flux), temperature exchanges (sensible heat flux) and momentum exchanges due to friction. The PBL is part of the troposphere, in which temperature steadily decreases with height (see fig. 2.5).

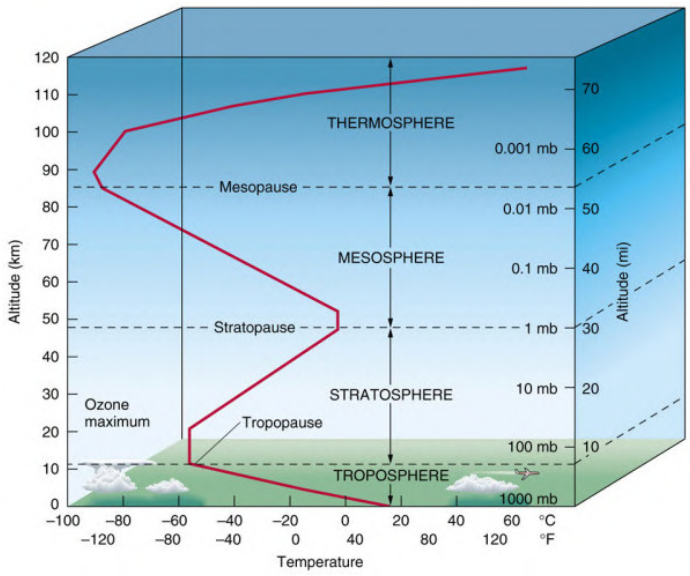

Figure 2.5: Schematic of the midlatitude temperature profile of the atmosphere.Reprinted with permission from StratusDeck (2021).

The troposphere is radiatively cooled by emitting more infrared radiation than it absorbs. The net radiative cooling of the atmosphere ($\sim$ -98 W/m^2) is primarily

balanced by latent heat release from water vapour (i.e., cloud formation, surface evaporation and precipitation). Turbulent processes incorporate tropospheric air into the PBL, such as daytime heating of land. This process of diurnal pumping is responsible of the varying depth of the PBL. Energy and moisture are transported out of the PBL through high cumulus clouds, known as cumulus convection (Randall, 2015).

The upper boundary of the troposphere is the tropopause at $\sim$ 17km from the surface. Here, the temperature is uniform with height. In the above lying stratosphere, temperature increases due to absorption of solar radiation from stratospheric ozone. At the 1 hPa level (about 50km height) lies the the stratopause, which denotes the beginning of the mesosphere. The decrease of ozone in this layer lowers the temperatures once again. The outermost layer, the thermosphere, is where space begins. The molecules in this layer absorbs the radiation and their excitement raises the temperature. For this thesis, only the lower two layers are of importance. At any given point layer in the atmosphere, temperature decreases with latitude and the meridional gradient is stronger in the winter hemisphere.

Surface boundaries

The GCA is strongly affected by the surface boundary conditions of Earth, since they exert different forcings. About 2/3 of Earth's surface are covered with oceans, which makes sea surface temperature (SST) a seasonally varying, lower boundary for the atmosphere. In general, Earth's surface is a huge source of moisture affecting the GCA through the large value of latent heat of water vapor. Its topography affects the GCA by exerting mechanical forcing through vegetation or mountains blocking winds, and thereby creating drag, as well as thermal forcing. The previously visited surface albedo prescribes the absorption of solar radiation of a surface. Especially land ice and and sea ice are not only a thermal boundary, but strongly affect the surface albedo, and by that the GCA. In fact, the GCA could be seen as a direction response to the boundary conditions (Randall, 2015).

2.3.2 Global circulations

Knowing the atmospheric structure and the role of the surface boundary, the following will tend to the main purpose of the general circulation of the atmosphere: the meridional (and upward) transport of energy, moisture and mass.

Moisture transport

In Earth's energy budget the latent heat is directly associated with surface moisture fluxes. The energy released in clouds from water vapour amount to 84 W/m^2, as shown in figure 2.1. The following will explain the connection in more detail.

The saturation vapour pressure, e_{sat}, determines how much water can be held by the atmosphere before it condenses and is strongly temperature dependent. On average an increase of 1 °C will increase the saturation vapour pressure by 6 %, which is why e_{sat} is larger in the tropics. In short, warm air is able to hold more water than cold air. The mixing ratio for water q_T vapour describes how much water can be held in a kg of air. If looked at it geographically distributed, the mixing ratio is greatest near the surface and in the summer hemisphere. Moreover, the most humid air is generally around the equator, while the driest air is located towards the poles. The commonly known variable relative humidity (RH), gives how close the air is to actual saturation in percent. The larger then percentage, the more humid it is. A full saturation will then lead to cloud formation and fog.

The transport of moisture can be derived from the continuity equation of water in z-coordinates. The following equation is the resulting transport of total water, converted into spherical coordinates, with zonal λ and long term mean t taken, vertically integrated and only dependent on latitude ϕ (Randall, 2015).

$$2\pi a\ cos(\phi) \int_0^\infty \overline{\rho_\theta \nu q_T}^{\lambda,t} d\theta = 2\pi a^2 \int_{-\pi/2}^{\phi} \left[\overline{(F_{q_T})_S}^{\lambda,t} - \overline{P}^{\lambda,t} \right] cos(\phi') d\phi' \tag{2.1}$$

Here, the left hand side is the total northward transport of moisture across latitude ϕ, $\overline{(F_{q_T})_S}^{\lambda,t}$ is the zonally average net evaporation and $\overline{P}^{\lambda,t}$ is the precipitation, at the surface.

The figure 2.6, shows the left hand side of eq. (2.1). Following the January moisture transport from left to right: (1) latent heat release from the Ferrel cell, (2) southward transport of moisture, (3) ITCZ - convergence of moisture , (4) diabetic heating from rain out/ condensation, or the uprising branch of the Hadley cell and (5) latent heat release around the roaring fourties.

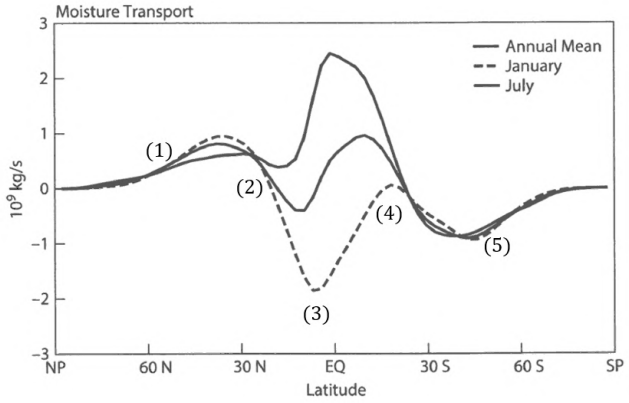

Figure 2.6: The vertically integrated, northward meridional moisture transport. Figure 5.7 from Randall (2015), adapted.

To examine the vertical distribution of the the meridional moisture flux, a stream function must be set-up, as shown in figure 2.7. Here, in January the moisture flows clockwise, opposite to the motion of dry air in the atmosphere. Only little poleward transport of moisture is vidible in the upper part of the Hadley cell. The stream function shows that moisture enter atmosphere via surface evaporation in subtropics and percipitates in the in the tropics of opposite hemisphere. At 60N the moisture flows into the ground due to the baroclinic systems.

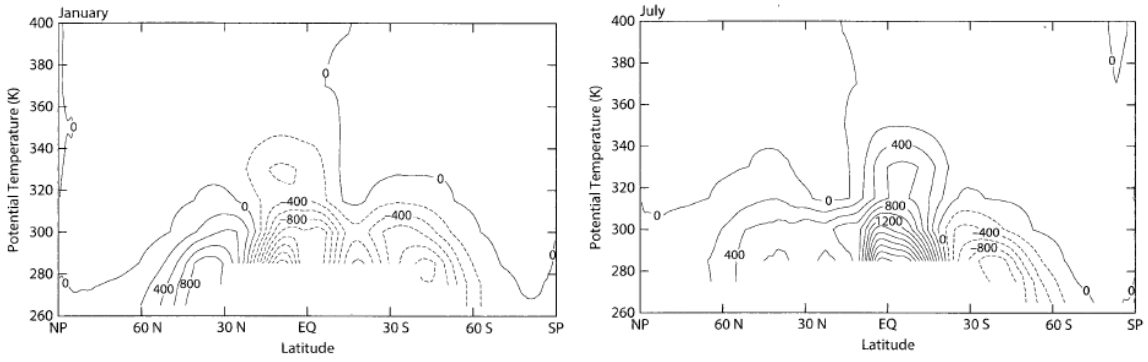

Figure 2.7: These plots show the streamfunction describing the atmospheric circulation of moisture in Januray and July. The sharp cut off comes from the ground and units are 10^6 kg/s. Figure 5.9 from Randall (2015).

Mass transport

Mass is one of the most fundamental quantities of the atmosphere, which can be described by the surface pressure. The surface pressure is equal to he weight of the air above per unit area. The surface pressure varies party due to the GCA and partly due to topography. To better observe horizontal pressure gradients often the mean sea level pressure (MSL) is used, which is the surface pressure without the impact of mountains. In the northern hemisphere (NH) winter there is a tendency for low pressure over land and high pressure over ocean and vice versa in summer, associated with the seasonal shift in surface temperature.

Similarly, the transport of mass across the equator varies with season and is related to temperature. A lower temperature will decrease the atmospheric depth, because cold air is more dense. This effect is compensated by the flow of pressure gradient force aloft, i.e. winds. For this reason, one can infer zonal mean winds from solemnly looking the atmospheric zonal average of temperature. Horizontal temperature gradients determine the velocity difference at different altitudes.

The mass of the atmosphere is greater in the winter hemisphere, since the effect of "dry" mass is larger than the negatively anomaly of water vapour. Nevertheless, globally speaking the whole atmosphere is heavier in NH summer due to the water vapour effect, as the surface temperature is increased by 3 °C.

Mass is transported through the atmosphere by winds, which are a characteristic feature of the atmosphere. The figure 2.8 depicts the general circulation developing from a state of rest into the three cells above. To demonstrate how these cells and winds are created, the following will explain the circulation cells. Each hemisphere consists of three so called circulation cells: the Hadley cell, the Ferell cell and the polar cell.

Due to the intense solar radiation, hot air rises at the equator taking up moisture from the ocean surface. The rising air cools and expands, forming a low pressure band with heavy clouds and precipitation, the Inter tropical Convergence Zone (ITCZ). The position of the ITCZ shifts seasonally, creating wet and dry seasons in the tropics. The rising air reaching the tropopause is advected poleward, since the stability of the tropopause is blocking any further vertical motion.Taking the NH as example: The coriolis force perturbes the northward air motion, such that the air is moving east ward when reaching about 30 N. The conservation of angular momentum increases the pace of the poleward wind. In combination, the increased speed and eastward motion creates the subtropical jet (jet stream).

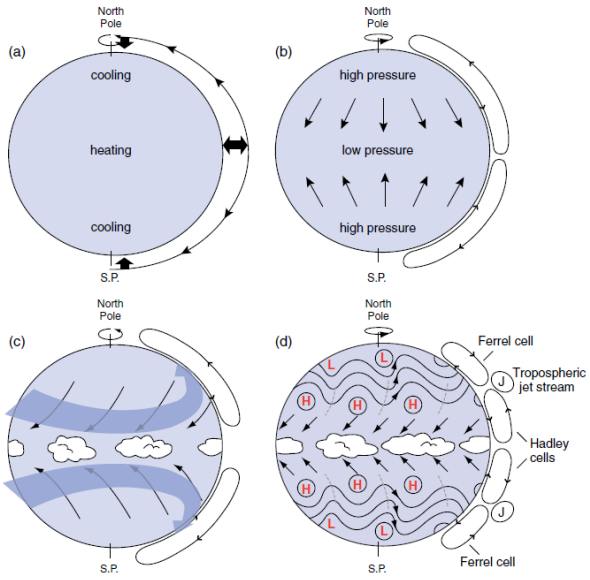

Figure 2.8: Schematic of general circulation developing from a state of rest. (a) the initial heating and redistribution of mass created pressure gradients leading to an equator-to-pole circulation cell (b). The coriolis force parts the large cell (c) until it is in balance with pressure gradient force, creating the cell schematic in (d). Figure 7.21 from Wallace and Hobbs (2006).

At 30N the poleward moving air piles up forming a high pressure at the surface. The subsidence in this region inhibits clouds formation and is he reason we find deserts form 30N and 30S. The air reaching the ground, turns toward the equator, forming trade winds that blow from northeast in the NH and southeast in the SH. This builds the Hadley cell in terms of mass. Its rising and sinking motion is oppositely in NH summer.

From 30N some of the diverging air moves poleward, gets advected due to the coriolis force and created westerly winds at the surface, again. At 60N the air rises creating precipitation clouds, known as the polar front. The air then return equator wards, building the Ferrel cell. Energy wise,the Ferrell cell motion is following the Hadley cell, creating a rising branch at 30N and radiative cooling/ sinking branch at 60N in NH winter.

The high pressure over the poles comes from sinking, warming air. At the surface the air moves again eastward due to the coriolis force and forms the polar easterly wind in the northern hemisphere. The cold polar air and warm subtropical air meet and form an air mass boundary , which is the polar front.

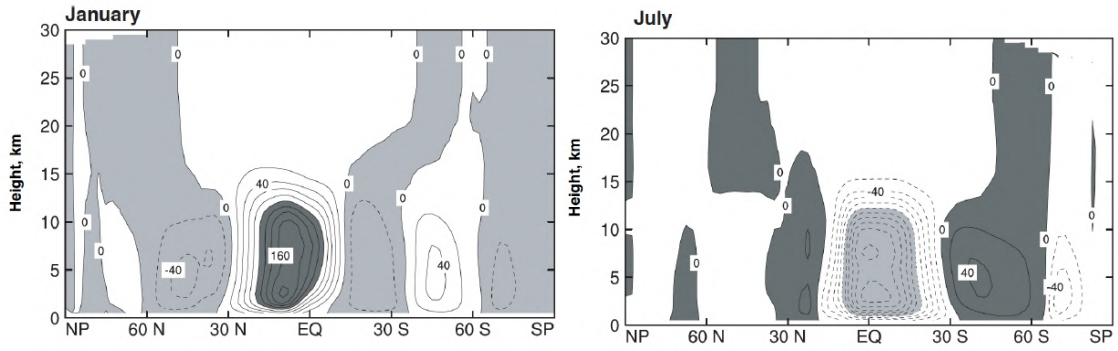

Figure 2.9: These plots show the latitude-height distribution of the streamfunction describing the atmospheric circulation of mass in Januray and July. Postitive values denote a clockwise circulation with units being 10^{12} g/s. Figure 3.17 from Randall (2015).

The mean meridional flow (MMC) can be derived from the continuity equation in pressure coordinates, which includes vertical velocity in pressure coordinates ω. As for the moisture circulation, a stream function showing the meridional flow of mass in the atmosphere can be set up (see figure2.9. The stream function shows the mass flows along the contours. The decrease of pressure with altitude represents the mass between two pressure surfaces.

The figure 2.9 shows a large Hadley cell at each Januray and July. with the raising branch in summer-hemisphere tropics and a sinking branch in in the winter hemisphere subtropics. A corresponding weaker hadley cell circulation is visble in the summer hemisphere. Both are direct circulationa, meaning the rising branch is warm and theri sinkinig branches are cool.

Energy transport

In general, the atmosphere tries to fight pressure gradients by tranportng energy (heat) poleward. The MMC can be observed in isentropic coordinates, so called Θ-coordinates. The potential temperature Θ can be used as a vertical variable such as height and pressure. In isentropic coordinates a parcel can only move between surfaces by diabetic heating or cooling. The MMC stream function in isentropic coordinates shows the energy flow in the atmosphere. The figure 2.10, shows a different picture than figure 2.9.

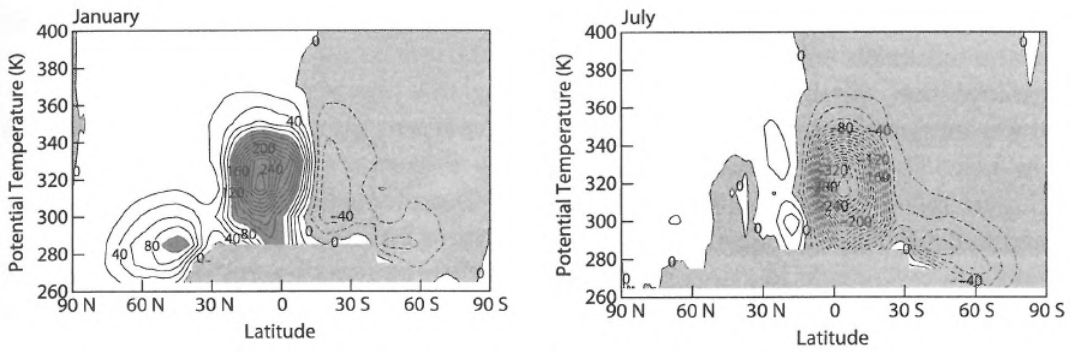

Figure 2.10: The streamfunction in isentropic coordinates showing the flow of energy in units 10^9 kg/s Figure 3.17 from Randall (Randall, 2015).

The rising branch of the Hadley cell is created through diabetic heating from latent heat release, i.e. condensation of water vapour. The sinking motion is due to radiative, diabetic cooling. In the NH winter the baroclinic instability due to larger temperature gradients entails many fronts and percipitation, and thereby release of latent heat. Atmospheric energy flows in NH winter are more vigorous and induce an indirect circulation, the Ferrell cell.

This baroclinic instability is a machinery that generates Rossby waves. The Rossby waves travel against the zonal mean flow of the jet stream, but relative to the zonal background flow which is overlaid by deviations from the mean flow. For long Rossby waves which move slower eastward than the short waves, atmospheric blocking occurs resulting in stationary weather. The wave energy is dispersed away from the mid latitudes in meridional direction.

A large and important step to enhance our understanding of the general circulation of the atmosphere, are general circulation models.

Chapter 3

Model and simulation set-up

This section describes the Earth System Model EC-Earth3, the albedo parameterization on which the sensitivity study is focused and the experimental set-up.

3.1 Earth System Models

Earth's complex climate system can be simulated through global climate models (GCMs), also known as general circulation models. These models use mathematical equations to describe the interaction of energy and mass with different components of the climate system: the atmosphere, the land surface and its vegetation, the oceans and sea-ice. In GCMs, the globe is discretized into 3 dimensional grid cells, each exchanging energy and mass with their neighbouring cells. GCMs are computationally costly due to their temporal and spatial resolution and are therefore run on High Performance Computers. Most GCMs have a coarse resolution compared to regional climate models (RCMs) which are down-scaled models suited for studies of regional phenomena and application to vulnerability, impacts and climate adaptation assessments. A new generation of GCMs are Earth System models (ESMs). ESMs are coupled climate models which include physical, chemical and biological processes, therefore reaching beyond their predecessors, GCMs, which just represented the physical atmospheric and oceanic processes. Earth system models are useful for sensitivity experiments since they allow for to exchange of energy, mass, aerosols, trace and greenhouse gases and nutrients between atmosphere, land and ocean, enabling the description of various feedback processes Döscher et al. (2022).

3.2 EC-Earth3

The model used in this thesis is the earth system model EC-Earth 3, v3.3.2. The model has been developed collaboratively by a consortium of 30 European research institutions from 12 different countries (the EC-Earth consortium). Based on the idea of combining numerical weather prediction (NWP) and global climate modelling, EC-earth was developed around 2006 with the weather forecast model of the ECMWF (European Centre of Medium Range Weather Forecast) as its base EC-Earth Consortium (2022).

EC-Earth is a modular ESM, meaning it can be run in different coupled configurations and allows the user to choose which climate feedbacks and processes to represent. In its most recent generation, EC-Earth3, the model includes components describing atmosphere, ocean, sea ice, land surface, dynamic vegetation, atmospheric chemistry, ocean biogeochemistry and the Greenland ice sheet (Döscher et al., 2022).

In this sensitivity study, EC-Earth3 is run in the atmosphere-standalone configuration, which is depicted by figure 4.1. The atmospheric model of EC-Earth 3 is originally based on ECMWF's Integrated Forecasting System (IFS) (ECMWF, 2021) - cycle 36r4, which is part of the operational seasonal forecast system S4. Many physical aspects of the original IFS were adjusted to run the atmospheric model for long climate simulations (e.g. decadal, centennial or longer) or simulations under different climate conditions (e.g. future scenarios or paleo simulations). A sub module of IFS is the land surface module Hydrology Tiled ECMWF Scheme of Surface Exchanges over Land (HTESSEL) (Balsamo et al., 2009). It solves all the atmosphere-land interactions by handling energy and moisture exchanges such as surface energy fluxes and soil moisture content.

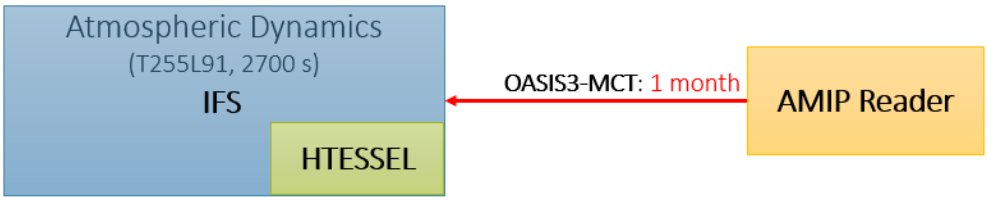

Figure 3.1: The EC-Earth3 climate model representing the atmosphere stand-alone configuration. In brackets the resolution and model timestep are shown. The red connection denotes the coupling timestep of the OASIS3-MCT.

In the atmosphere-standalone configuration the ocean model NEMO3.6 (Gurvan et al., 2022) with its integrated sea-ice sub module LIM3.6 (Rousset et al., 2015) as well as the fresh water runoff mapper are replaced by an interface called the Atmospheric Model Intercomparison Project (AMIP) reader.

The AMIP reader takes 1x1 deg monthly sea surface temperature (SST) and sea ice (SI) concentration fields from the CMIP6 provided AMIP data sets which are composed based on observations. Further, the AMIP reader applies linear temporal interpolation and sends the resulting daily fields to IFS. Lastly, the OASIS3-MCT (short for "Ocean Atmosphere Sea Ice Soil") coupling library handles the communication and interpolation of data between different model components and grids. Simulations in this atmosphere-standalone configuration of EC-EARTH3 are often referred to as AMIP experiments or IFS-only experiments. For simplicity, the latter is chosen as naming for this configuration from here on.

As shown by figure 3.1, IFS and the included HTESSEL are run at T255 spectral resolution with a linear reduced Gaussian grid, which globally corresponds to a horizontal resolution of $\sim$ 80 km, and 91 vertical levels.

3.3 Snow albedo parameterization

The sensitivity study focuses on the global impacts of the new snow albedo parameterization introduced into EC-Earth3 by Madsen et al. (2021). This albedo scheme is worked into the land surface model HTESSEL. Therefore, the following will give a brief introduction into HTESSEL and detailed description of the standard and new albedo parameterization. The description and equations of HTESSEL and the standard parameterization will closely follow the IFS documentation from ECMWF (2021).

3.3.1 HTESSEL

The land surface and soil hydrology model HTESSEL is a sub module of IFS that solves the energy and water balance at the land surface using four vertical layers to represent the soil temperature and moisture. For each grid point of IFS, the land surface is represented by six different land surface types (tiles): bare ground, low and high vegetation, intercepted water, shaded and exposed snow (Döscher et al., 2022). Over sea, freshwater and inland water bodies, the tiles are categorized into open or frozen water (ECMWF, 2021). Each land-surface tile has its own properties, describing the heat, water and momentum exchanges with the atmosphere.

3.3.2 Surface energy balance

As mentioned above, each land surface tile in HTESSEL calculates the energy balance and surface temperature (skin temperature T_{sk}) individually to account for its own surface features. The radiative surface fluxes are expressed as area weighted averages over the tiles. Moreover, only the variables describing the specific humidity, the atmospheric temperature and wind speed are commonly shared by all tiles. The energy balance for a specific tile, with index i, follows as:

$$(1 - f_{Rs,i})(1 - \alpha_i)R_s + R_{LW,i} + H_i + L_{v,s}E_i = \Lambda_{sk,i}(T_{sk,i} - T_1) \tag{3.1}$$

where:

R_s	downward short-wave radiation
R_T	downward thermal radiation
σ	Stefan-Boltzman constant
T_1	temperature of upper soil/snow layer
H_i	sensible heat flux
$L_{v,s}E_i$	latent heat flux from skin layer (v:evaporation, s: sublimation)
$\Lambda_{sk,i}$	skin conductivity
$(1 - f_{Rs,i})$	partial absorption of net short-wave radiation remainder passed to soil/snow
$R_{LW,i} = \varepsilon(R_T - \sigma T_{sk,i}^4)$	net long-wave radiation (ε: long-wave emissivity)
$(1 - \alpha_i)$	absorption of R_s governed by surface albedo α_i

The net long-wave radiation R_{LW} will be reevaluated after the energy balance calculation to take into account the shift in skin temperature due to surface exchanges. The resulting R_{LW} is used in further calculation to estimate the energy transferred to other surface processes ECMWF (2021). For most tiles the surface albedo is set to a constant and thereby highly parameterized. The exception is snow covered tiles. In the following sections the snow albedo parameterization will be described.

3.3.3 The standard snow albedo scheme

HTESSEL includes a straightforward snow model, that represents a single snow layer on top of the upper soil layer for snow tiles. This snow layer is identified by a single snow temperature T_{sn} and snow mass S. Moreover, heat fluxes are calculated throughout the snow pack. Its density evolves over time and its capacity to hold liquid water is approximated as a function of density and snow mass Dutra et al. (2010). If the snow pack absorbs energy, the T_{sn} changes which can lead to snow melt if T_{sn} exceeds the melting point ($T_{sn} \geq T_f - d/2$, with T_f being the triplet point of water and $d = 4$K).

For this specific snow pack, the snow albedo (α_{sn}) varies over time following the equations given by Baker et al. Baker et al. (1990).

$$\alpha_{sn}^{t+1} = \begin{cases} \alpha_{sn}^{t} - \tau_a \Delta t/\tau_1 & M_{sn} = 0 \\ (\alpha_{sn}^{t} - \alpha_{min}) \exp(-\tau_f \Delta t/\tau_1) + \alpha_{min} & M_{sn} > 0 \quad \text{or} \quad T_{sn} \geq T_f - d/2 \end{cases} \tag{3.2}$$

Here, the snow albedo decreases exponentially under melting conditions ($M_{sn} > 0$) and linearly under non melting conditions ($M_{sn} = 0$). Moreover, the timescale $\tau_a = 0.008$ decreases the albedo by 0.1 in 12.5 days, $\tau_1 = 86400$s (length of 1 day) and $\tau_f = 0.24$ gives an e-folding time of ~ 4 days. When fresh snow falls, the albedo adapts accordingly. If the snowfall rate (F) exceeds a given threshold of 10 kg/m^{2}h, the snow albedo reset to a maximum value such that $a_{max} = 0.85$, which can be seen in equation (3.1). Here, the model time step (in hours) is represented by Δt.

$$\alpha_{sn}^{t+1} = \alpha_{sn}^{t} + \min\left(1, \frac{F\Delta t}{10}\right)(\alpha_{max} - \alpha_{sn}^{t}) \tag{3.3}$$

However, for areas of thick perennial snow, i.e. areas where the snow depth reaches above 9 m or more, the snow albedo is set to a constant value ($\alpha_{per} = 0.80$). These conditions prevail over ice-sheets, such that the time-varying albedo is not used over for example the Greenland ice-sheet and is in fact constant over it. The maximum thickness of 10m is set in place to preserve conservation of water. If snow falls on ice-sheets of maximum thickness, the excess is added to the ocean as calving.

3.3.4 New albedo parameterization

The albedo parameterization in the standard set-up of EC-Earth3 sets a constant albedo ($\alpha_{sn} = 0.80$) over perennial snow, and thereby ice-sheets (see section 3.3.3). This fails to account for the seasonal cycle of albedo as well as the important ice/snow-albedo feedback. A more sophisticated albedo scheme was recently introduced into EC-Earth3, which is described as the «Albedo Scheme Copenhagen (Cph)» by Helsen et al. (2017).

In a joint effort of improving the surface mass balance (SMB) of the Greenland ice sheet within EC-Earth, a new land surface type - ice sheet - was introduced into HTESSEL. This surface type is applied via a mask and is technically not a tile. The mask is constructed by taking the global snow depth variable from the initial files and dividing it by 10. When the value in the mask is larger or equal to 0.9 (corresponding to a 9 m snow thickness) for a certain grid point, the new albedo parameterization is applied and overwrites the underlying tile albedo. It should be noted that HTESSEL is not able to distinguish between snow and ice or simulate snow grain size, such that the new albedo parameterization has the standard scheme (described in 3.3.3) as its base.

The new scheme replaces the constant albedo by a time-evolving one, using the equation 3.3 and 3.2 with different values. The Copenhagen albedo scheme uses the same maximum albedo value ($\alpha_{max} = 0.85$) as before. During no melt conditions, so called dry conditions, a slow exponential decay of albedo is applied, to include the slow effect of dry snow ageing.

$$\alpha_{sn}^{t+1} = (\alpha_{sn}^{t} - \alpha_{firn}) \exp(-\Delta t/\tau_{firn}) + \alpha_{firn} \tag{3.4}$$

This equation decays towards a minimum firn albedo ($\alpha_{firn} = 0.75$) with a e-folding time $\tau_{firn} = 30$ days. During wet conditions, presence of liquid water due to melting ($T_{sn} > -1.99°\text{C}$) or rainfall, the albedo is immediately set to the minimum albedo value ($\alpha_{min} = 0.60$).

$$\alpha_{sn}^{t+1} = \alpha_{min} \tag{3.5}$$

Under wet conditions albedo decays faster. The effect in eq. (3.5) accounts for water filling the space in between the grains and thereby immediately increasing the effective grain size, as well as acknowledging water as a strong accelerator for grain growth (Helsen et al., 2017). A switch between wet and dry conditions resets the albedo to $\alpha_{refrozen} = 0.65$ to highlight the low albedo of refrozen melt water. It should be noted that the snow albedo does not directly depend on temperature, as seen in both eq. (3.5) and eq. (3.4), which physically is the case.

3.4 Simulation set-sup

As a means to study the impact of the new snow albedo parameterization, several IFS-standalone simulations were performed. The decision to not use the ocean and atmosphere coupled version of EC-Earth3, allows to study the observed changes more thoroughly since less processes are involved. Moreover, the runtime in the IFS-standalone configuration is faster and computationally less costly.

The simulations are divided into three experiments with each three members, as can be seen in Table 3.1. The members only differ in their initial states, so called AMIP realizations, which allow for different climate paths during the simulations. The first experiment contains three control simulations [CTRL] using the standard albedo parameterization, the second experiment contains three perturbed simulations with the new albedo parameterization [LANDICE] and the third experiment contains three extreme simulations [EXTRM] with a constant albedo of 0.6 over perennial snow. For the third experiment, a new variable was integrated into IFS to lower the albedo while keeping the original mask set-up.

Experiment	**Members**	**AMIP realization**
CTRL	1-CTRL	r5
	2-CTRL	r8
	3-CTRL	-
LANDICE	1-LANDICE	r5
	2-LANDICE	r8
	3-LANDICE	-
EXTRM	1-EXTRM	r5
	2-EXTRM	r8
	3-EXTRM	-

Table 3.1: Overview of IFS stand-alone simulations. The third AMIP realization has no official name.

The simulations 1-CTRL and 2-CTRL were performed by Shuting Yang and the remaining 7 simulations by the author. A combination of all members of one experiments into an ensemble is referred to as: All-CTRL, All-LANDICE or All-EXTRM.

The albedo parameterization was applied to everywhere above 60° southern latitude to exclude Antarctica. One reason for this exclusion are the much colder temperatures over Antarctica, which leads to an extremely slow snow metamorphism (Wang and Zender, 2011).

As mentioned in section 3.3.4, the new parameterization is accessed via a mask. For the run 1-LANDICE the mask is shown in figure 3.2, where every grid point with more that 9 m of snow thickness (values ≥ 0.9) uses the new albedo scheme. These grid points are colored white in the fig. 3.2, illustrating that the parameterization is mainly affecting the Greenland ice sheet (GrIS), Ellesmere island and surrounding Nunavut, Iceland and Svalbard.

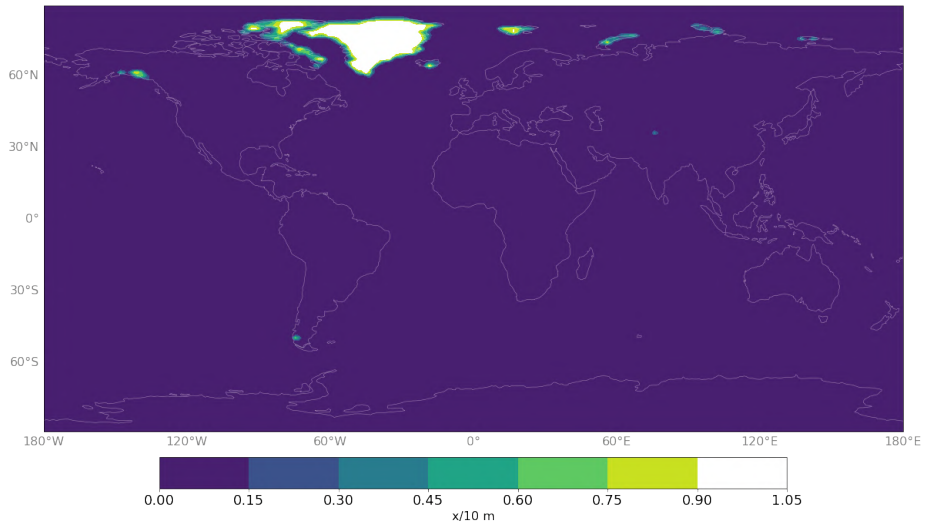

Figure 3.2: Mask for albedo parameterization of run 1-LANDICE. This mask was created from the initial snow depth from the 01.01.1970. Values above 0.9, corresponding to 9m snow thickness the new albedo parameterization is used.

The mask is used further to define surface properties. For values larger than 0.5 in the mask (corresponding to 5 m of snow thickness), the heat conductivity as well as the surface roughness lengths are changed for the underlying tile.

It should be noted, that the mask is created from the initial snow depth from the 1st of January 1970 (i.e., the starting the of the run). Since all three experiments are started on different initial climate states the extent of the mask slightly differs between the LANDICE simulations. However, this effect is only minor and the affected areas are the same.

Each simulation ran for 49 years on the supercomputer environment hpcdev. The time span of the simulation was from 1970 to 2018, of which 9 years were taken away for the spin-up of EC-Earth3. The result and analysis sections discuss thereby data

over the timespan 1979-2018, or 40 years.

Chapter 4

Data Handling and Statistics

Most variables of the EC-Earth3 output were post-processed into netCDF 4 files. These were analyzed using the climate Data operator (CDO) and using python. The following section deal with the statistical significance testing of the data.

4.1 Statistical significance testing

When introducing a new parameterization, as it is done in this thesis, it is important to know whether this change produces a significant difference or a random pattern. The first approach was to divide the distributions by their standard deviation to get a feeling for the strength of the response to the modification of the model when comparing the means. However, this division is not sophisticated enough since it fails to give insight about the statistical significance of the difference. For instance, in a large data set the difference in means can be small compared to the standard deviation and still very significant or vice versa. Thus, two different statistical tests were chosen to compare the EC-Earth data. The first test is the Welch's t-test, which asks whether the two distributions have significantly different means. The second test is the Kolmogorov-Smirnov test, which inquires if two distributions are significantly different. The following will discuss the theory behind these tests.

4.1.1 Welch's t-test–unequal variance t-test

The two-sample Welch's t-test is an adaptation of the common Student's t-test which allows for unequal variances. This is important for comparing our climate data, since the variances are overlapping due to high point correlation between the samples. To begin with, a meaningful hypothesis is set up (null hypothesis) for two given samples X and Y. These samples are assumed to be dependent (paired), normally distributed and are allowed to differ in size. In this case, the null hypothesis states that there is no difference between the two population means. As described above, the standard deviation, σ, is not a good measure for the significance of a difference of means, but the so called standard error, s, is. The standard error of the mean measures the dispersion of sample means around the population mean. Commonly, the standard error equals the sample's standard deviation divided by the square root of number of points in the sample (Steel et al., 1997). The appropriate s_d is computed as follows,

$$s = \sqrt{\frac{\sigma_X^2}{n_X} + \frac{\sigma_Y^2}{n_Y}}, \tag{4.1}$$

where σ^2 is the standard deviation and n is the size of the population. Now, the t statistic is the difference in sample means divided by s_d, as in Eq. (2.2) (Press et al., 1992).

$$t = \frac{\overline{X} - \overline{Y}}{s}. \tag{4.2}$$

The calculated t value is then compared to tabulated values to find a corresponding probability lying between 0 and 1. A low probability corresponds to a high significance, meaning the null hypothesis is rejected. In the opposite case, the means of the two distributions are not significantly different and the null hypothesis is accepted.

4.1.2 Kolmogorov-Smirnov test

The two-sample Kolomogorov-Smirnov (K-S) test asks whether two sets of data, X and Y, are drawn from the same distribution or not. This test is known to be non-parametric, meaning the data points do not need to be sampled from a gaussian or otherwise defined distribution. In general, the K-S test compares the empirical cumulative distribution function of two samples by estimating their separation. The empirical cumulative distribution function for a sample of size n is defined as,

$$F_X(x) = \frac{1}{n}\sum_{i=1}^{n} 1_{[-\infty,1]}(X_i), \tag{4.3}$$

where $1_{[-\infty,1]}(X_i)$ is the indicator function, equal to 1 if $X_i \leq x$ and equal to 0 otherwise (Storch and Zwiers, 1999). The resulting graph is a step function, which increases by a step of 1/n for each observation. Comparing the two different cumulative distribution functions $F_X(x)$ and $F_Y(x)$ (of sample size n and m), leads to the K-S statistic:

$$D_{X,Y} = max_x|F_X(x) - F_Y(x)| \tag{4.4}$$

The figure 4.1 shows the Komogorov Smirnov statistic D, which denotes the largest distance between the two cumulative distributions.

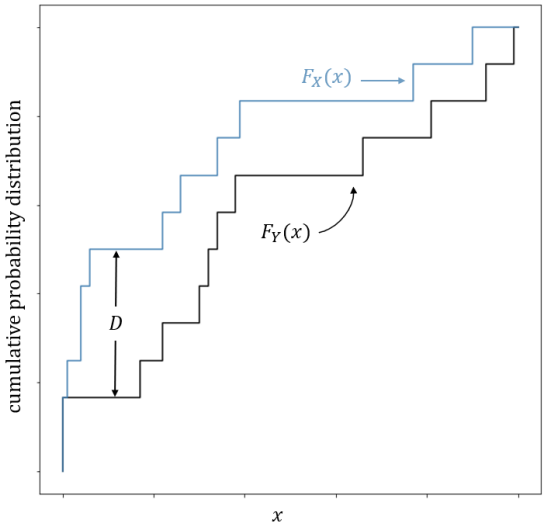

Figure 4.1: Kolmogorov-Smirnov statistic D for two sample test. Both step functions are constructed to rise equal amounts each time.

The null hypothesis (samples are drawn from the same distribution) is rejected at a certain significance level, α, if:

$$D_{X,Y} > c(\alpha)\sqrt{\frac{n+m}{n \cdot m}}. \tag{4.5}$$

The value of $c(\alpha)$ can be taken from common literature tables. For our case, a significance level $\alpha = 0.05$ was chosen such that $c(0.05) = 1.36$, which is an adaptation to the values presented by Miller (1956) for $n \leq 40$.

4.1.3 Comparison of significance tests

The testing of significance was done by comparing the time series of each grid point. The atmospheric EC-Earth3 output is placed on a gaussian grid of size 512x256, resulting in 131071 grid points. The time series were either 40 year seasonal or annual means. To increase the importance of the reponse, the datasets were concatenated into three runs of the same type such that timeseries are then larger datasets of 120 points. For the testing, built-in python function were used to create masks of significant points and the significant areas were marked through hatching. The two function used are:

- `scipy.stats.ttest_ind(X,Y,equal_var=False,alternative='two-sided')`
- `scipy.stats.ks_2samp(X,Y,alternative='two-sided')`

To estimate the significant percentage of the results, each grid point was weighted by the cosine of the latitude, $\cos(\phi)$.

Some precautions are needed to be done when comparing the results. Both the K-S–test and Welch's t-test assume the data points to be independent, i.e. uncorrelated. However, when testing local significance of climate data, as it is done in this thesis, grid points are highly correlated. Significant grid points will be gathered into coherent areas, since the temperature in one grid point will be influenced by it neighbouring points and vice versa. In detail, a local warming in one point will also cause warming in the neighbouring points. This may lead to an overestimation of the significance of a perturbation through underestimating the variance of the perturbation response. The implications of this are visited later in the results section, with larger focus on the decrease of degrees of freedom (df).

The K-S–test and Welch's t-test both show similar significant areas but differ in their extent. In a direct comparison of the significant areas through histograms, it is visible that the K-S–test has stricter requirements than the t-test. In other words, the t-test is easier to cheat or it is easier to make type I and II errors. Type I errors are also known as false positive, meaning the null-hypothesis is rejected even though there is no significant difference between the data sets. The type II error is its counterpart, leading to false negatives or accepting the null hypothesis even though there is a significant difference in the time series.

Since the comparison of the tests showed that both tests indicate the significance of the perturbation response similarly, it was concluded that the K-S–test is too strict for the perturbation applied in this thesis. Therefore, the Welch's t-test was chosen

to analyze the results for a simpler comparison. The less strict requirements on this test should be taken into consideration when interpreting the results.

Chapter 5

Results & Analysis - local

This section analyses the local results, which include the observed changes in snow albedo and radiative fluxes. Local in this case means changes in the area where the new snow albedo is set.

5.1 Effective changes in snow albedo

In order to see the local effect of the new albedo parameterization, the simulated GrIS snow albedo α_{sn} was compared to the Moderate Resolution Imaging Spectroradiometer product (MODIS, Box et al. (2017)). The MODIS satellite product contains daily snow albedo data from 2000-2017 for the GrIS.

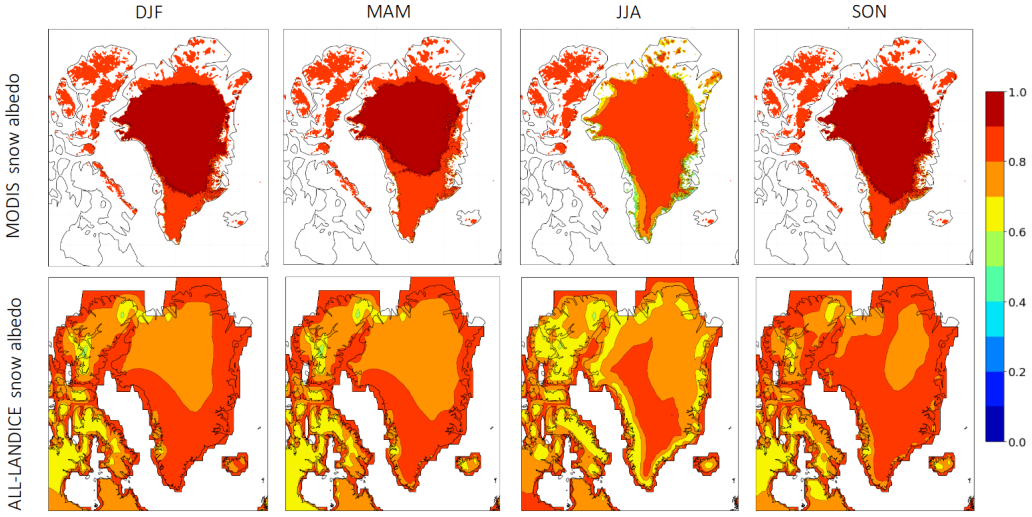

Figure 5.1: Seasonally average snow albedo over the Greenland Ice sheet between 2000-2017. Upper panel shows the observed MODIS snow albedo, the lower panel shows the simulated snow albedo of All-LANDICE.

The figure 5.1 shows the simulated snow albedo of all LANDICE simulation combined (All-LANDICE) and the MODIS snow albedo, averaged over seasons. In general, the All-LANDICE snow albedo exhibits a seasonal cycle over perennial snow, showing that the new albedo scheme is responsive compared to the constant albedo $\alpha_{sn} = 0.8$ of the CTRL experiments (see figure 5.2).

Even though the flexibility and ability to respond to changes in temperature and precipitation is advantageous, the figure 5.1 shows deficits of the new snow albedo scheme. In direct comparison to the observed data, the simulated snow albedo shows a cold bias towards the northern dry area of the ice sheet, whereas the albedo of the 3-CTRL simulation seems to overall match the MODIS data better.

The MODIS snow albedo is less constrained than the All-LANDICE albedo, which can be explained by the coarse resolution of EC-Earth3. A lesser constraint scheme may lead to large areas of under- or overestimation of snow albedo, which would produce an erroneous simulation of the snow albedo.

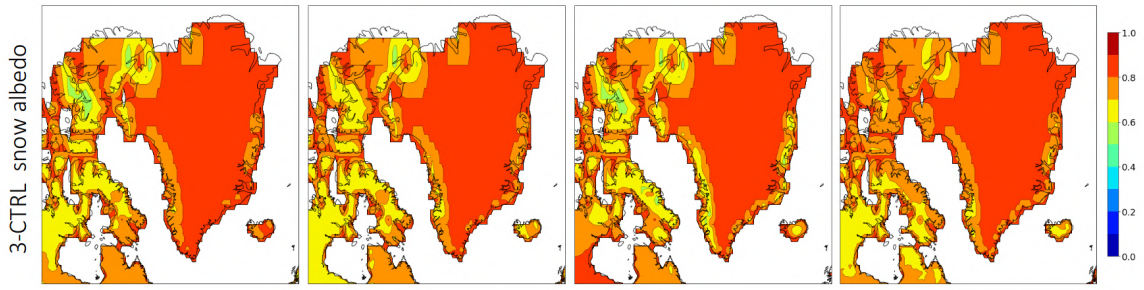

Figure 5.2: Seasonally averaged snow albedo over the Greenland Ice sheet between 2000-2017. Panel shows simulated snow albedo of 3-CTRL.

From figure 5.1 it can be seen that the All-LANDICE ensemble underestimates the northerly snow albedo in all seasons. Table 5.1 gives an overview of the seasonal mean α_{sn} between 2000-2017, showing that the snow albedo is 11% lower in all seasons aside from summer. One reason for this underestimation could be the timescale of the dry ageing being too short. This would result in a too fast decay towards the minimum firn albedo under dry conditions.

Season	**Modis α_{sn}**	**All-LANDICE α_{sn}**
DJF	0.89	0.78
MAM	0.87	0.76
JJA	0.79	0.75
SON	0.88	0.77
Annual average	0.86	0.77

Table 5.1: Seasonal averages of snow albedo over the GrIS and Ellesmere island from 2000-2017. The last row shows the annual average of the time span.

The high albedo in the southern part of Greenland could be attributed to more snowfall towards the south. Looking at the zonally averaged snow fall in figure 5.3, the simulation All-LANDICE shows larger values of snowfall to the south in most seasons. This observation overlaps with the simulated seasonal albedo evolution shown above.

The study by Helsen et al. (2017) confirms that EC-Earth can capture the snowfall over Greenland well. The simulated dry areas in central as well as northern Greenland, the snow fall maxima in the south east and the snow fall minima along the western ice sheet margin agree fairly well with observational data. However, the lower resolution of EC-Earth3 causes larger zones of maximum snowfall, leading to an overestimation of snowfall over the southern GrIS. Since large snow fall rates reset the albedo to the maximum of 0.85, this reset increases the albedo towards the southerly perennial snow of the GrIS.

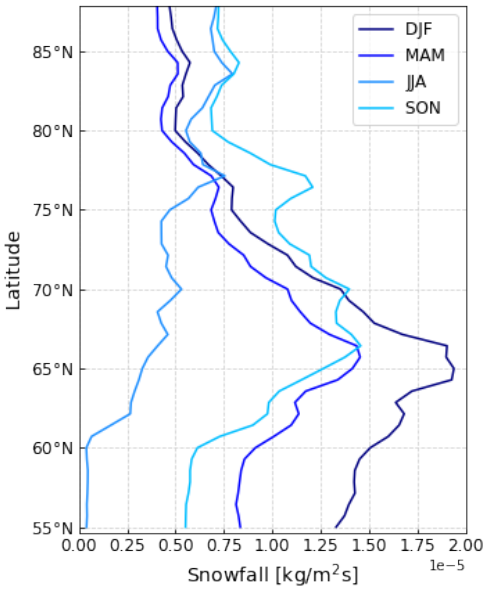

Figure 5.3: Zonally averaged snowfall of All-LANDICE over Greenland and Ellersmere island. Zonal means for 2000-2017 average over seasons.

Towards the ablation zone, especially in the summer season, the snow albedo pattern is comparable to the MODIS data. Observed values of the average snow albedo in the JJA season lie between 0.75-0.8 (Helsen et al., 2017). In figure 5.4, the average JJA snow albedo over the entire GrIS is compared between the observed data and All-LANDICE simulation. As seen here, the simulated JJA snow albedo hits the lower margin of reported observations with an average of $\alpha^{\mathrm{JJA}}_{1-\mathrm{LANDICE}} = 74.8\%$, $\alpha^{\mathrm{JJA}}_{2-\mathrm{LANDICE}} = 75.0\%$ and $\alpha^{\mathrm{JJA}}_{3-\mathrm{LANDICE}} = 74.9\%$, compared to $\alpha^{\mathrm{JJA}}_{\mathrm{MODIS}} = 79.1\%$.

The MODIS time series also shows the minimum average summer albedo recorded in 2012 with a value of 76.6%, corresponding to the record year of maximum melt extent. The year 2000 marks the record high of the JJA albedo with 80.5%. Even though the simulations are forced by observed sea surface temperature (SST) and sea ice concentration (SIC), these features are not visible in the simulation of the JJA snow albedo. This shows that the model has biases. Moreover, the variability in the simulated snow albedo is less than in the MODIS albedo, which could be due to the constraint of the snow albedo parameterization.

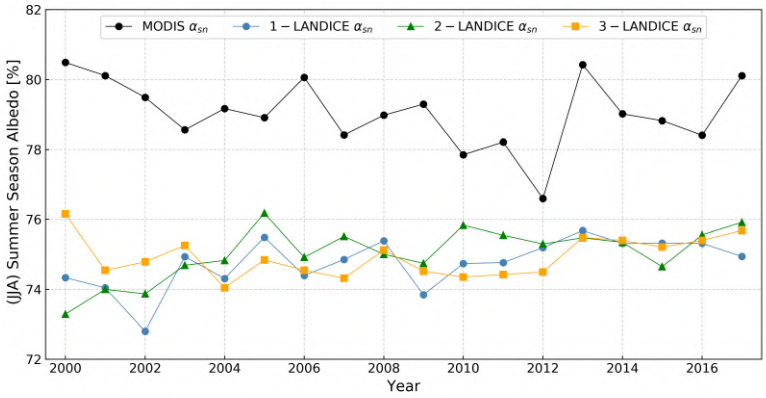

Figure 5.4: Timeseries of summer season (JJA) albedo , averaged over Greenland and Ellesmere Island between 2000-2017.

To take a closer look at what influences the JJA snow albedo, two grid points were chosen to do an in depth study. Figure 5.5 shows the time series of the snow albedo and the snowfall for each grid point respectively. The snow melt, or run off, in these points is not shown because it is equal to zero. This means there has been little to no melt in both points in the JJA seasons between 2000-2017. The point A is located in the northern dry area and the JJA snow albedo decreases over time. Since there is no snowfall or run off over the time span, the main process decreasing the albedo may be the dry ageing.

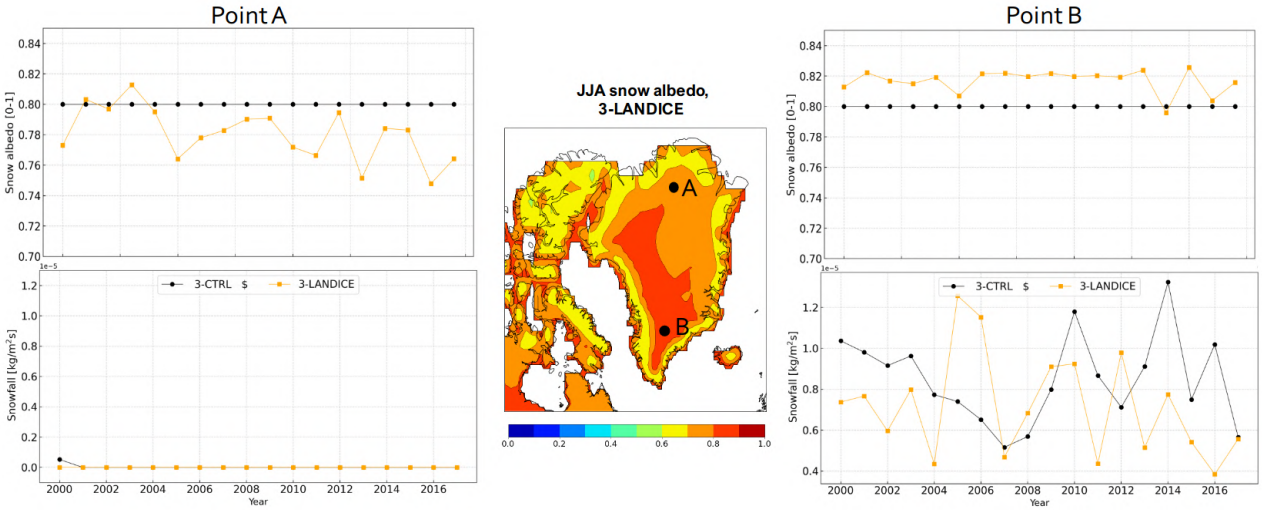

Figure 5.5: Timeseries of summer season (JJA) albedo and snowfall for two grid points between 2000-2017. Run off is not shown, since it is euqal to 0 in both grid points.

Over point B, the albedo seems to be stable at around 0.82. This would mean there is an interplay between the reset of snow and the dry ageing, since the albedo doesn't follow the snowfall rate exactly and there is no run off. The plot emphasizes that the snowfall has an influence on the snow albedo, aiding the previous hypothesis that the snow albedo is higher in the southern part of the GrIS due to the snowfall reset.

The values shown in the time series are means over the JJA season, however most processes affecting the snow albedo change on shorter timescales. Moreover, the snow has the ability to store some liquid water which is not set to the run off. This would induce wet conditions that effectively lower the albedo. To better pin point the processes that affect the albedo and its variability in the simulation, further investigation should be done.

To summarize, a seasonal cycle of snow albedo has been introduced over perennial snow by making the albedo scheme more responsive to changes temperature and precipitation. On an annual average, the simulated α_{sn} is about 9% lower than the MODIS observation. The bias over the northern dry areas shows that the albedo scheme may need some improvements such that the dry conditions to match the observational data better. Overall, the albedo is higher toward the southern part of the GrIS due to more snowfall in that area, showing the influence of precipitation to the new albedo scheme.

5.2 Surface energy fluxes

The net surface solar radiation (SSR) –the difference in incoming to outgoing short wave (SW) radiation, is governed by the surface albedo. Together with the net long-wave (thermal;LW) radiation (STR) at the surface, they combine to the net radiative surface fluxes. From now on these will be referred to as net radiative fluxes. Since the response of the LANDICE runs is locally very similar, the LANDICE and CTRL runs have been concatenated into "mini" ensembles each containing 3 runs of the same type. The idea behind this follows that any reoccurring pattern from the albedo perturbation will be more recognizable in the combination of runs.

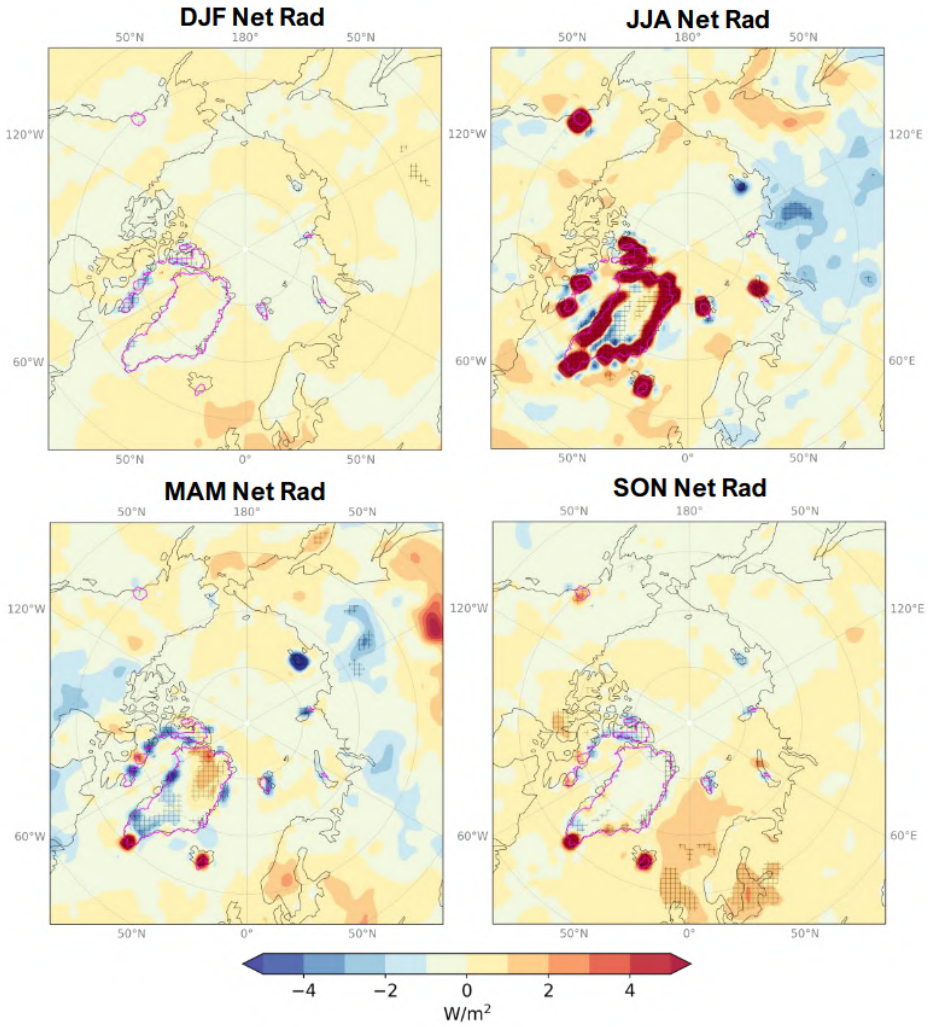

Figure 5.6: The response of the net radiation at the surface (SW+LW) seasonally averaged over the years 1979-2018 (All-LANDICE - All-CTRL). Positive values correspond to a downward direction. The hatching indication regions of statistical significance (at significance level $\alpha = 0.05$). Net negative anomalies cool the surface and near surface temperature. The pink contours indicate the mask of the new albedo scheme.

The figure 5.6 represents the net radiative flux response of the All-LANDICE ensemble compared to All-CTRL ensemble, seasonally averaged over 1979-2018. The pink contours on the plots show the areas where the new albedo scheme is applied, highlighting that only a few areas have been perturbed in the LANDICE runs. The new parameterization scheme allows for higher maximum values than the standard set-up. However, as visible from table 5.1, the annual mean albedo is lower than 0.8 for all LANDICE simulations, averaging at 0.77. This results in an overall larger uptake of solar radiation where the albedo scheme is applied.

Due to the lack of insolation during the northern hemisphere winter, the local net radiation changes are negligible in this season (December-February,DJF). A significant impact of the new albedo scheme can been seen in the spring season (March-Maj; MAM), especially over Greenland. The previously described snow albedo bias towards the northern part of GrIS, is directly visible the MAM response. The positive anomaly indicates a larger uptake of energy by the surface, thereby warming and melting snow over the ice sheet. As discussed in the previous section, the larger values of precipitation towards the south allows for higher albedo values, and thereby increasing the cooling towards the south of the GrIS. The changes in net radiative flux, where the albedo scheme is applied, equal -0.18 W/m^2, representing an overall cooling in spring.

Since most radiation is available in the summer season, the largest local impact on the net radiative fluxes from the new snow albedo is expected here. The strong warming seen in the summer (June-August, JJA) is due to the seasonal melt at the ice sheet margin and where the albedo scheme is applied. The available solar radiation in this season drives the strong seasonal melt patterns, as well as the precipitation at the margins. Over the parameterization mask an increase in net radiative fluxes of 8.10 W/m^2 is calculated for JJA. The Fall season shows a small change of -0.12 W/m^2.

The response of the turbulent surface fluxes, surface sensible heat flux (SSHF) and latent heat flux (SLHF), is shown in figure 5.7. Here, negative anomalies warm the surface, relating directly to the observations done for the net radiative fluxes above. Most outstanding is the coherent positive anomaly bordering the Norwegian coast line in Autumn. The significant anomaly corresponds to a cooling that continues into the winter season. Since the boundary conditions are the same between the runs, this anomaly must be atmospherically driven. Moreover, this significant increase in turbulent heat fluxes might indicate a time lag in the response, since the largest local impact of the snow albedo parameterization is during summer.

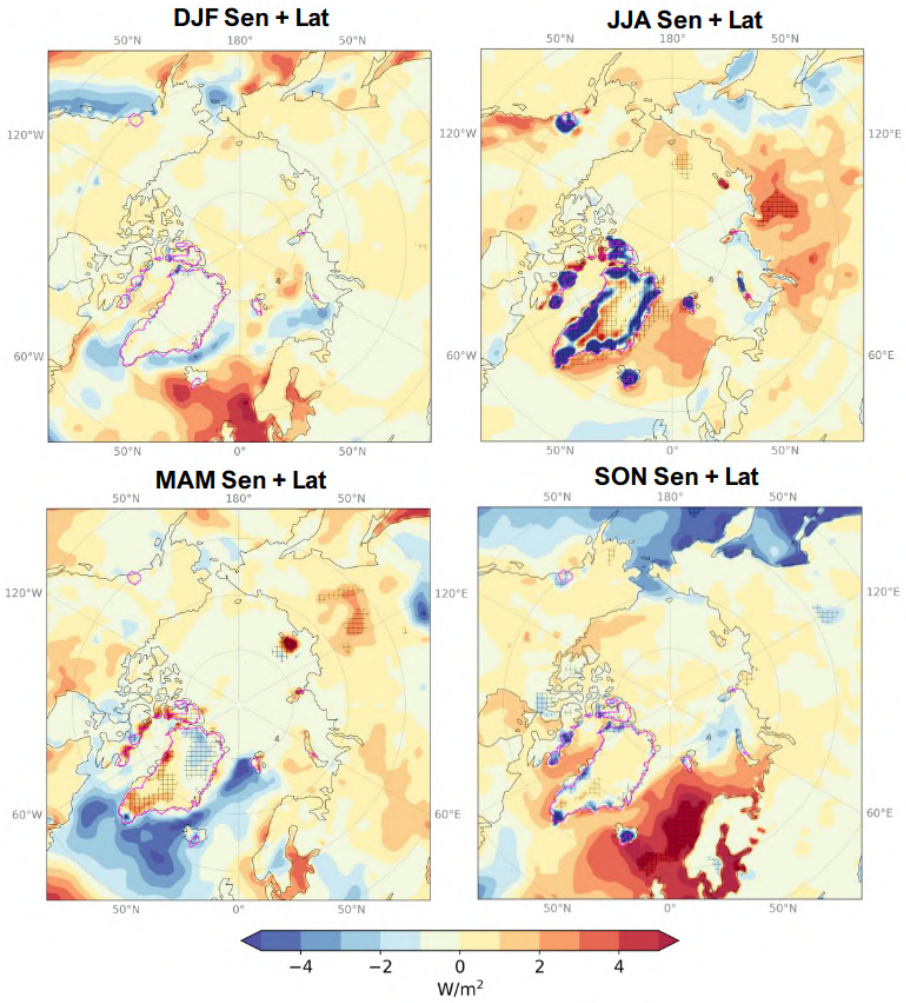

Figure 5.7: The response of the turbulent heat fluxes at the surface (SSHF+SLHF) seasonally averaged over the years 1979-2018 (All-LANDICE - All -CTRL). Positive values correspond to a upward direction. The hatching indication regions of statistical significance (at significance level $\alpha = 0.05$). Net negative anomalies warm the surface. The pink contours indicate the mask of the new albedo scheme.

To investigate this anomaly further, the standard deviation over the All-CTRL ensemble during the fall season is observed (see 5.8). The benefit of looking at the standard deviation of the ensemble, is that the variability between the members as well as the interannual variability is included. The variability of the surface turbulent heat fluxes is large over the northern hemisphere. However, in front of the Norwegian coast line the variability is smaller than in other regions, making it more likely to see significant changes. The strong positive anomaly seen in figure 5.7 amount to maximum 20% of the standard deviation, which is still relatively small. This hints that strong coherent signal might arise from random processes.

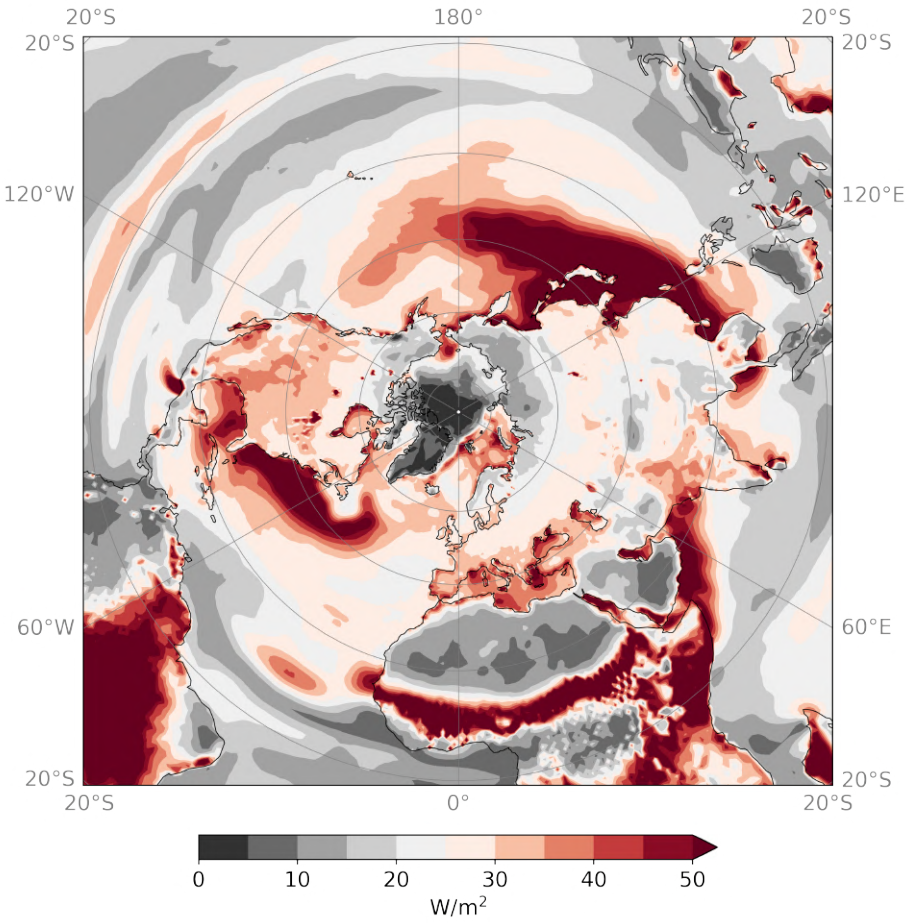

Figure 5.8: The standard deviation of the SON SLHF+SSHF taken over the All-CTRL ensemble.

In figure 5.9 the evolution of the surface energy components over Greenland and Ellesmere island is shown. The figure displays that the applied forcing in the LANDICE simulations is overall small leading to little changes compared to CTRL runs. The fluxes behave as expected towards the forcing, showing a larger uptake of energy from the surface with more available solar radiation. And thus, an increase in turbulent fluxes and OLR. The spread between the members is very small and therefore only their mean is shown.

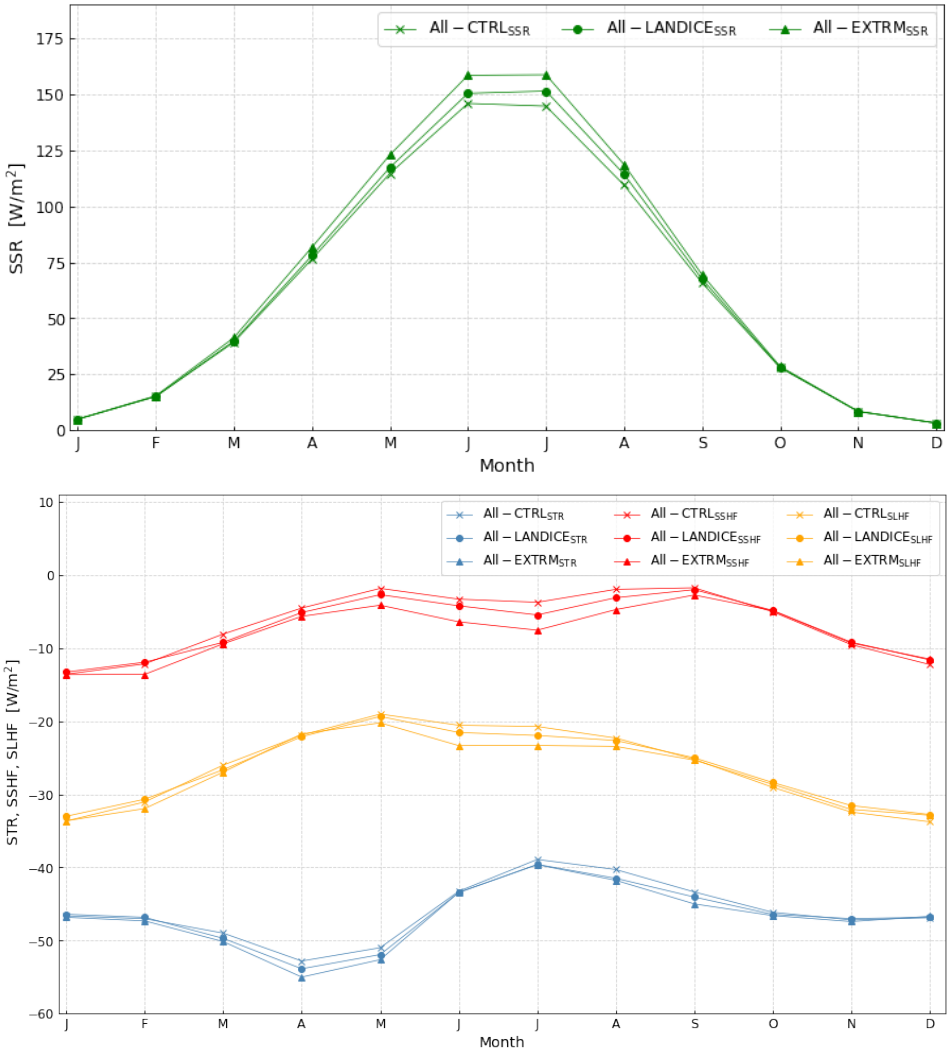

Figure 5.9: Evolution of All-LANDICE, All-EXTRM and All-CTRL ensembles over Greenland and Ellesmere Island. Months are average over 40 years between 1979-2018.

To quantify the effect of the new albedo scheme, the annual mean contributions to the surface energy balance have been calculated over the parameterization mask. The reason for only including the area where the new albedo scheme is applied, was to measure the direct forcing. In table 5.2, the annual mean contributions are shown. As expected the largest difference is visible in the net surface solar radiation with an increase of 2.43 W/m^2, confirming the new albedo scheme leads to more radiation uptake of the surface. The response in the All-EXTRM case is large due to the very low albedo, and as expected strongest in the SSR. Overall, the annual local mean forcing at the surface from the albedo perturbation amounts to 0.68 W/m^2 and 2.23 W/m^2 for the extreme case.

Radiative flux	**All - LANDICE**	**ALL-EXTRM**	**All -CTRL**
SLHF	-1.53	-7.03	-0.95
SSHF	17.91	10.61	18.55
SSR	26.36	45.55	23.90
STR	-40.61	-46.99	-41.14
Sum fluxes	1.60	3.15	0.92

Table 5.2: Average surface energy balance over the parameterization mask. Values represent the longterm mean in W/m^2.

All in all, the new albedo parameterization has a local effect on the surface energy balance leading to and increased uptake of energy by the surface. The seasonal changes directly relate to the albedo changes discussed in the previous section. The in situ annual impact is estimated at 0.68 W/m^2 for the LANDICE perturbation. However, the changes on the surface energy components through the perturbation are small. The turbulent heat fluxes show a significant positive anomaly during autumn, but the anomaly is small in raltion to variability of the area.

Chapter 6

Results & Analysis - remote

6.1 Temperature

The 40 year annual mean difference in near surface temperature between 1-LANDICE and 1-CTRL can be seen in figure 6.1. It shows a clear pattern of alternating warm and cold anomalies. Around Greenland, the largest differences originate from the seasonal melt showing strong warming spots around the ice sheet margin. The revision of the snow albedo scheme leads to a better representation of melt in the ablation areas of the GrIS (Helsen et al., 2017), which is directly visible in the figure.

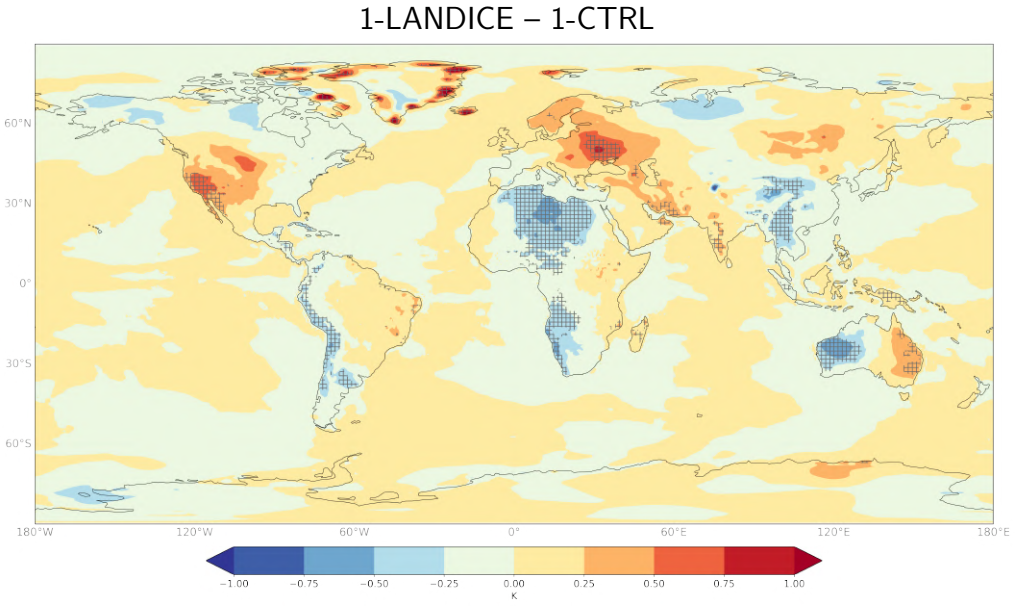

Figure 6.1: The difference in annual mean T2M (1-LANDICE - 1-CTRL) for 1979-2018. Hatching indicates significance at a 95% significance level. Anomaly pattern shows a 4.8% significant difference.

The temperature changes over the perennial snow of the GrIS can be further related to the changes in net radiation at the surface and the simulated albedo show in

section 5.1. The lower albedo in the norther dry area leads to an in increased T2M. The opposite holds for the southern part of the GrIS, leading to colder near surface temperatures.

The T2M pattern shows a significant 0.5 to 1 degree warming in the western to central U.S., over eastern Europe and eastern Australia. Similar significant cooling is visible at the western border of South America over the Andes, straight throughout the African continent, south-east Asia and western Australia.

The results in figure 6.1 show a 4.8% significant difference (with significant points weighted by latitude). At a 95% significance level significant, differences are expected to occur about 5% of the time. This would imply that the anomaly pattern shows less significant points than a random perturbation. However, the Welch's t-test assumes the grid points to be uncorrelated, which is not the case for climate data. Correlation leads to a decrease in degrees of freedom (df). Nonetheless, all runs are similarly perturbed meaning the decrease in df should be similar too. This implies that the applied snow albedo perturbation should have no large effect on the total amount of df, especially since polar regions have less df than the tropics. This similarity argument validates the significance of the pattern even though it is under the 5% threshold. Nevertheless, only a small part of the perturbation response exhibits a significant difference. On a similar note, one can observe areas of little change in temperature, which indicate a significance, e.g. over Indonesia and Papua New Guinea. These significant areas are meaningless and arise solemnly due to randomness.

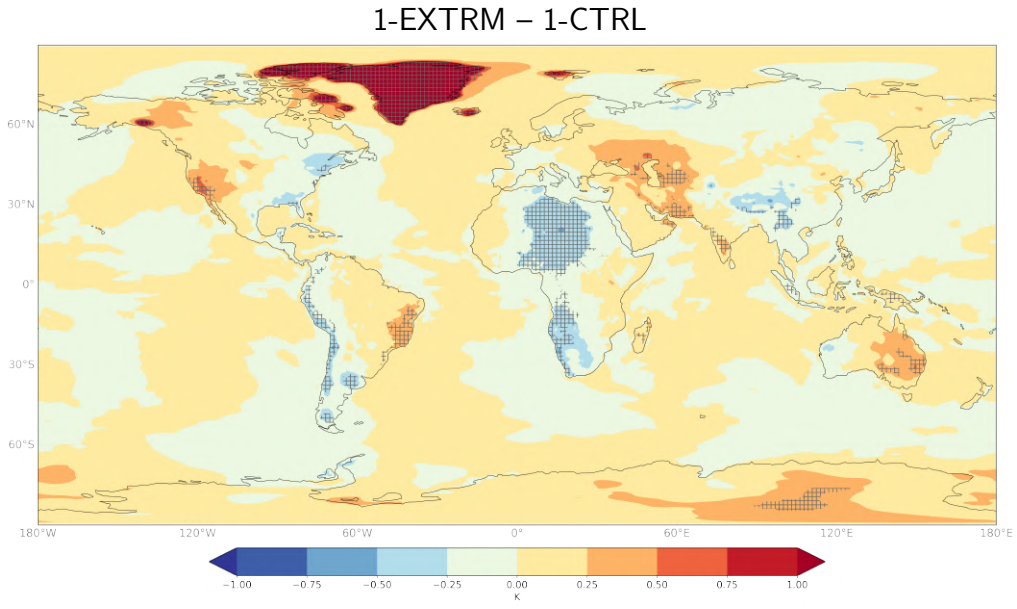

Figure 6.2: The difference in annual mean T2M (1-EXTRM - 1-CTRL) for 1979-2018. Hatching indicates significance at 95% significance level. Anomaly pattern shows a 4.5% significant difference.

The alternating temperature pattern persists when comparing the 1-CTRL run to the 1-EXTRM run. Even though the temperature differences are in the same places, the warming and cooling anomalies are weaker in the extreme case. The most outstanding is the persisting cold anomaly stretching straight through the African continent, exhibiting a large area of statistical significance. The dark red areas indicate where the extremely low albedo was set, showing a large increase in near surface temperature due to the albedo reduction.

Taking a closer look at large deviations from the mean, a strong but small negative anomaly is visible near the Tibetan Plateau. This anomaly does not stem from the new albedo parameterization since the snow depth of that glacier does not exceed 9 m (as it can be seen from the mask in figure 3.2). As described in section 3.3.4, the mask is used to define surface properties which results in the observed negative anomaly.

Comparing the second members of Experiment 1 and 2, a similar pattern of alternating warm and cool spots is visible, along with the same cooling anomalies over the African continent, the Andes and south-eastern Asia (see figure 6.3a). The extreme comparison is shown in the Appendix A.1, with comparable results to figure 6.1.

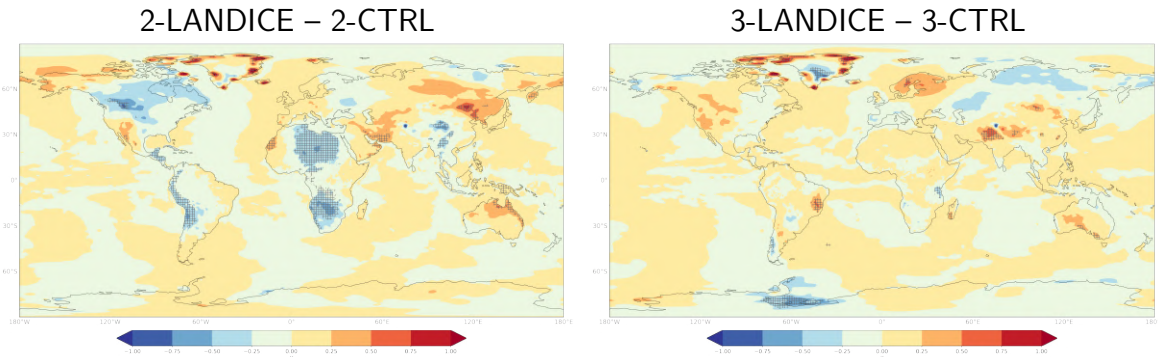

(a) **(b)**

Figure 6.3: The difference in annual mean T2M between a) 2-LANDICE - 2-CTRL and b) 3-LANDICE- 3CTRL for 1979-2018. Hatching indicates significance at 95% significance level. Anomaly pattern shows a 4.5% significant difference in (a) and 1.1% in (b).

The impact of the albedo parameterization when comparing 3-LANDICE and 3-CTRL is presented in figure 6.3a, with the extreme case shown in appendix A.2. Surprisingly, the alternating pattern vanishes for both cases. The large warm anomalies in 1-LANDICE – 1-CTRL and 2-LANDICE – 2-CTRL are now cooling anomalies. Moreover, the cold anomaly over the GrIS as well as the seasonal melt is enhanced compared to the other comparisons. The results of figure 6.5a are statistically similar, since they only show a significant difference of 1.1% for 3-LANDICE – 3-CTRL and 1.4% for 3-EXTRM – 3-CTRL .

This lack of robustness of the near surface temperature response hints that the annual remote anomalies are most likely due to the large internal variability of the atmosphere and not induced by the applied snow albedo parameterization. The internal variability is the natural climate variability that occurs as a consequence of intrinsic processes of the atmosphere. Looking at the runs as ensembles containing three members of the same type, i.e All-LANDICE, All-CTRL and All-EXTRM, the results above show two individual members agreeing with the pattern and one not.

Climate change projections are often based on multiple simulations of a GCM forming large ensembles, where the degree of consensus of the members can be mapped as member spread. Also there, distinguishing between the lack of consensus between the members and the lack of signal is difficult especially considering the internal variability. In studies by Landrum et al. (2012) on global sea ice concentration, the large inter-annual variability produces trends that were only statistically significant for 2 out of 6 ensemble member. Using an ensemble run of a GCM with 24 members Zunz et al. (2013) modelled the Southern ocean sea ice extent, reporting that only some memebers reproduce the increase in sea ice extent similar to observations. Their response difference is again largely attributed to the role of the internal variability.

Tebaldi et al. (2011) showed the lack of member agreement on precipitation projection could be connected to large noise from the internal variability masking the signal. This highlights another important fact. A change can be significant in a statistical sense, but this does not imply it overcomes the internal variability. Meaning that even though significant changes are visible in the T2M, it is hard to distinguish the changes from the internal variability with only using three members or looking at their comparison individually. Similar issues were reported by Ogawa et al. (2018), when linking Arctic sea ice loss to northern hemisphere winter climate change. The study emphasizes that perturbations in the T2M are best captured with as many models as possible forming a multi model ensemble. Therefore, to better judge the albedo influence on a global and annual scale, many more simulations need to be conducted forming much larger ensembles.

The comparison of All-LANDICE and All-CTRL shown in figure 6.7b, highlights the low amplitude of the induced anomalies. Most of the T2M anomalies (apart from local anomalies over the GrIS) do not exceed 0.5K.

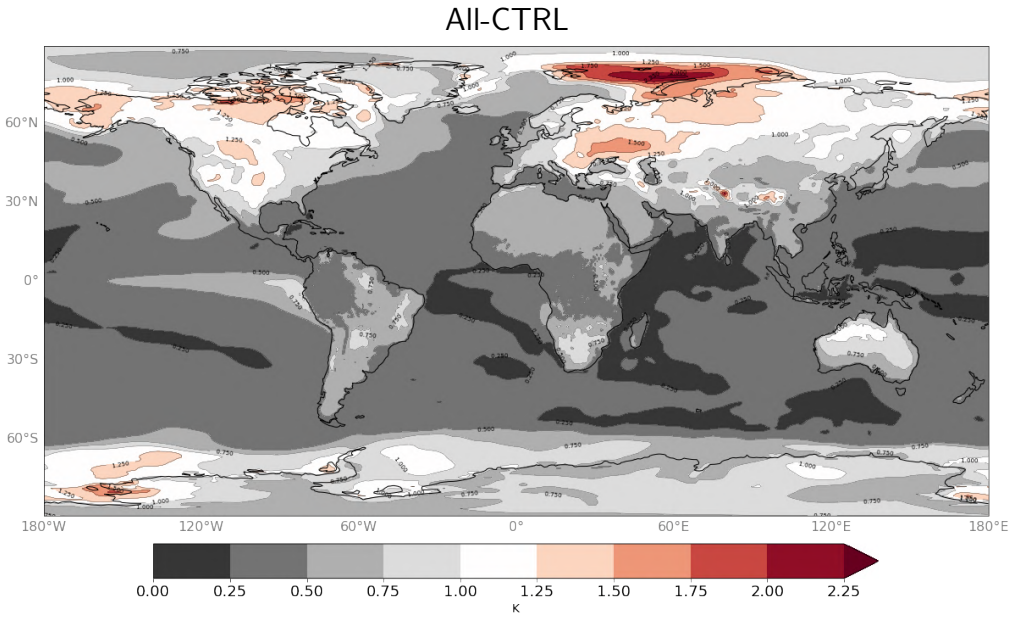

Figure 6.4: The standard deviation for the All-CTRL ensemble. Standard deviation taking over the annual means of the entire ensemble.

The annual mean standard deviation in T2M of the All-CTRL ensemble is shown in figure 6.4. It can be seen here, that the observed T2M anomalies on the SH amount to half of the standard deviation of the CTRL runs. However, the variability on the SH is low making it more likely for significant differences to occur. The variability increases towards the northern high latitudes, most likely masking any perturbation impact across the NH. Finally, in figure 6.5 the CTRL runs are compared. The plots show that the remote anomaly pattern can arise due to the internal variability of the model with equal strength and significance, by only comparing the CTRL runs.

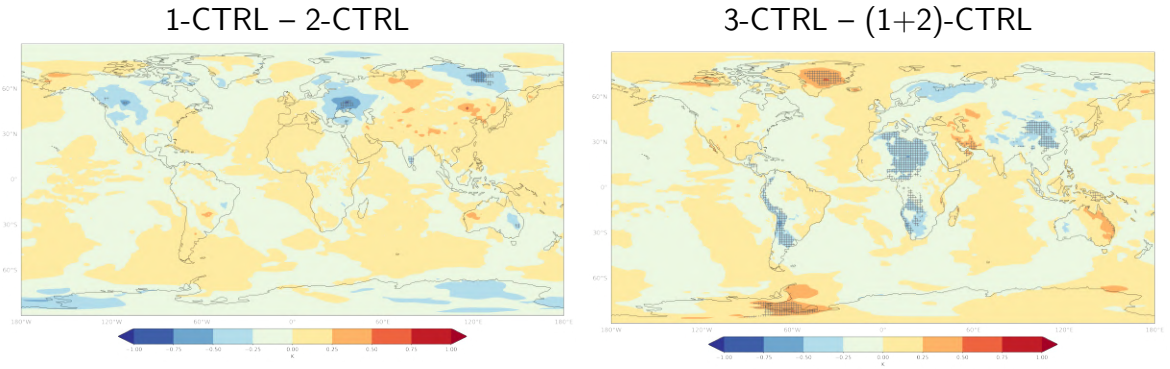

(a) **(b)**

Figure 6.5: The difference in annual mean T2M between a) 1-CTRL – 2-CTRL and b) 3-CTRL– (1+2)-CTRL for 1979-2018. Hatching indicates significance at 95% significance level. Anomaly pattern shows a 0.3% significant difference (a) and 5.2% in (b).

This emphasizes that the remote T2M response can be attributed to the large internal variability and the induced anomaly pattern arises due to the randomness of the atmosphere. However, this does not mean that the albedo parameterization has no impact at all, but that its remote influence is relatively small and is most likely overwritten by the chaotic processes of the atmospheric circulation, on a global scale and over annual averages. This result makes sense in relation to how small the applied forcing and the adjusted area is.

The further investigation will keep the ensemble structure to observe potential significant changes. Further, down scaling to seasonal averages increases the chance to see an influence of the albedo forcing since its impact is largest during summer and spring.

From the background review in section 2, it is known that the snow albedo its feedback follows a seasonal cycle with the strongest SAF response in the NH spring season. The 40 year seasonally averaged response of All-LANDICE runs compared to All-CTRL runs can be seen in figure 6.6.

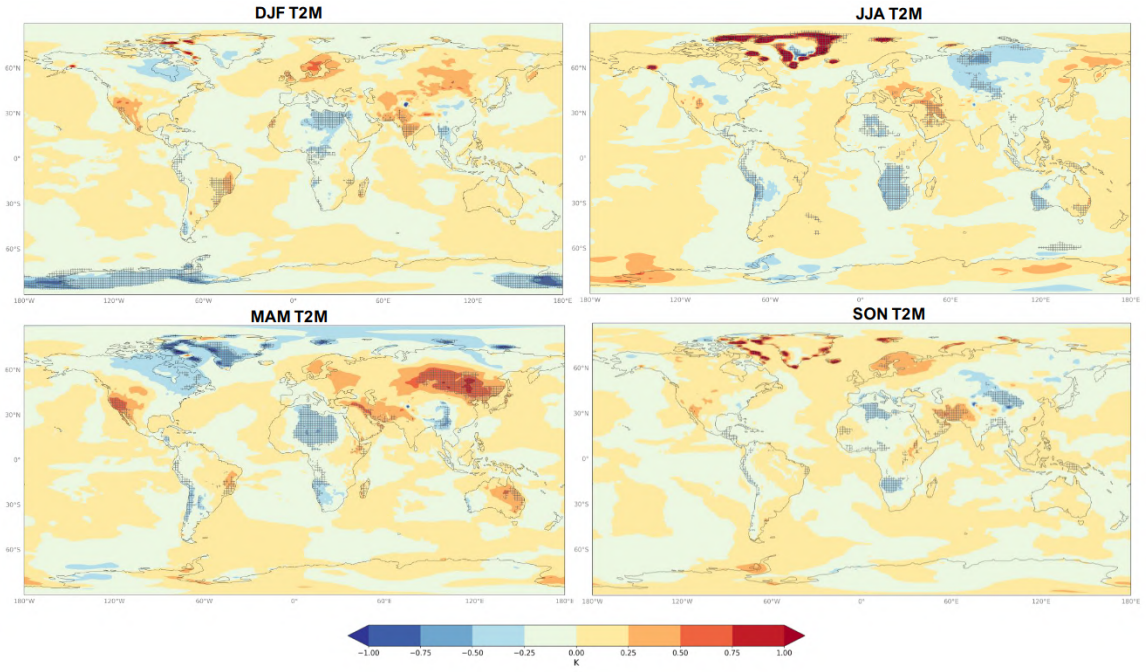

Figure 6.6: The difference in seasonal mean T2M (All-LANDICE- All-CTRL) for 1979-2018. Hatching indicates significance at 95% significance level. Anomaly pattern shows a 3.9% significant difference in DJF, 6.0 % in MAM, 5.7% in JJA and 3.7% in SON.

As expected, the remote pattern from the observations persists, which can be connected to internal variability. Therefore, the analysis concentrates on changes in the northern hemisphere, especially close to where the new albedo scheme is set. The winter season anomalies are mostly weak and insignificant due to the lack of insolation

in NH winter at high latitudes. Visible changes in the winter season are presumably not radiatively driven, since the surface albedo perturbation has little to no effect on the surface energy budget. This emphasizes that the winter season anomaly pattern must be induced by other processes or be random. However, a small but significant warming is visible over Scandinavia.

The spring response shows a large cold anomaly over the GrIS and Nunavut,Canada. This local change could be related to the new albedo scheme raising the albedo towards the southern part of the ice sheet above 0.8. The increase albedo reflects more solar radiation in the LANDICE runs than in the CTRL runs with a constant albedo $\alpha_{sn} = 0.80$. The lowering of T2M in this region is consistent with the observation of changes in regional radiative fluxes in the previous section also relating to the applied forcing in spring. Moreover, there is a consistent warm anomaly over Siberia, which will be revisited later. The summer season exhibits large seasonal melt patterns, which continue into the fall season. Moreover, a significant cooling anomaly is visible over northern Siberia which might be induced by the albedo perturbation. During the fall, some significant warming is visible over Scandinavia, which ties into the winter season. The seasonal T2M comparison for All-EXTRM in reference to All-CTRL is shown in the figure A.3. It displays the remote pattern similarly to figure 6.6, however in this comparison significant changes are mainly seen over Greenland and Ellesmere island.

To summarize, the global and annual response in near surface temperature to the new snow albedo parameterization produces an anomaly pattern of which the remote anomalies can be attributed to the large internal variability of the atmosphere. Looking at the variability of the CTRL runs and comparing the CTRL runs with each other, shows that the remote anomaly pattern can arise solemnly through their comparison. The member spread of the CTRL simulations as well as the inter annual variability increases towards the northern hemisphere, decreasing the chances to see any significant differences. Over seasons, the northern hemisphere response shows a few significant patterns over Scandinavia and northern Siberia, which are not found in the extreme comparison. A strong local response is seen where the albedo perturbation is set. The response shows strong anomalies in spring, leading to colder T2M over the GrIS and north-east Canada, as well as strong seasonal melt is visible at the ice-sheet margins especially in summer.

6.1.1 Temperature bias

Changes in near surface temperature, or two meter temperature (T2M), relate directly to changes in the atmospheric pressure and thereby its general circulation patterns. The snow albedo has a large effect on the regional and near surface temperature in the cryosphere through the SAF. However, many climate models fail to represent the snow albedo evolution, overestimating the NH winter albedo (Li et al., 2016). A more realistic snow albedo that removes this bias should lead to a better estimation of the T2M.

To see if the new albedo scheme would affect the T2M bias of EC-Earth3, the All-CTRL ensemble is compared to ECMWF's ERA-5 reanalysis data over the time span 1979-2018. Reanalysis data is a combination of global observations and model data to provide a complete picture of past and current climate.

The figure 6.7a shows the large model bias of EC-EARTH3 with temperature anomalies ranging between ± 6 K. In the performance analysis of EC-Earth3 conducted by Döscher et al. (2022), an overall 0.5 K warm bias has been reported in comparison to ERA5 T2M. Here, an ensemble of historical simulation was used, following the CMIP6 protocol. The Coupled Model Intercomparison Project (CMIP) is a standard framework for studying coupled GCM's in simulations of past, present and future climate.

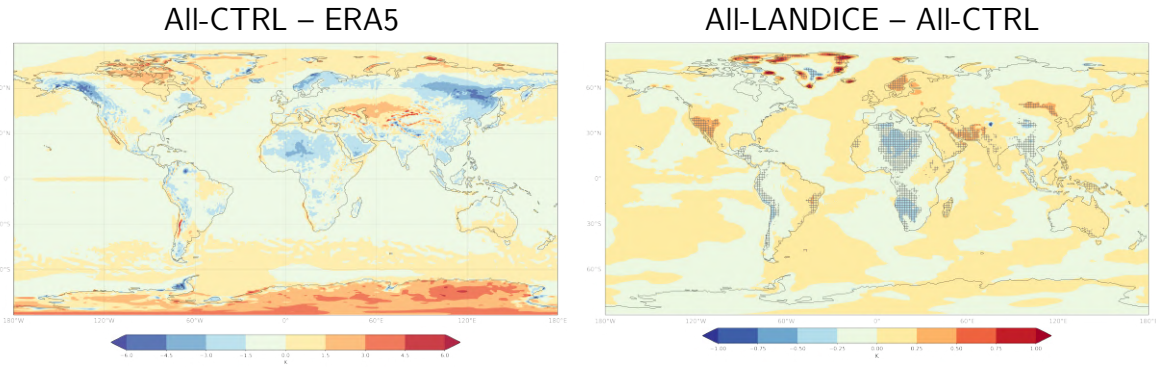

(a) **(b)**

Figure 6.7: Comparison to ERA5 reanalysis data. The figure (a) show the large model bias, while figure (b) shows the T2M anomalies between ALL-LANDICE – ALL-CTRL. The hatched areas indicate significance at the 95% level, with 6.3% of the results being significantly different in (b). No hatching in (a), since the bias is large.

For the period 1980-2010, Döscher et al. found a cold bias over the Arctic and a warm bias over Antarctica and Southern ocean. Moreover, the member spread was found to be larger in the northern hemisphere than in the southern hemisphere. In figure

6.4 a similar behaviour can be seen, as the difference in standard deviation between All-CTRL members is larger on the NH. However, the direct bias comparison between 6.7a and Döscher et al. will differ, since this simulation uses the IFS-only configuration and is the coupled model.

Similar to the findings in the EC-Earth3 performance study, figure 6.7a shows a warm bias over the northern high latitudes and a cold bias over the southern low latitudes. The T2M anomalies between the All-LANDICE and All-CTRL ensembles are shown in figure 6.7b with values ranging between $\pm$ 1 K. The new parameterization would only make minor contributions to reduce any remote biases, since the amplitude of the remote response is very low in figure 6.7b and not necessarily showing the forced response. Over the Greenland and Ellesmere island, the new parameterization would reduce the cold biases at the ice sheet margins and over Ellesmere island. Moreover, the new parameterization lessens the T2M bias over the perennial snow, reducing the warm bias in EC-Earth3. However, this reduction might be too strong in over the southern part of the ice sheet Overall, the new albedo parameterization will lead to local bias reductions for the simulated T2M of the EC-Earth3 atmosphere-standalone configuration.

6.2 Mean sea level pressure & geopotential height

In this section the response of the mean sea level pressure (MSL) and the 500 hPa geopotential height (GPH) to the albedo forcing is studied. As discussed in the previous section, large remote changes can be attributed to the large internal variability of the atmosphere. Therefore, this section concentrates on seasonal anomalies over the northern hemisphere, which can be seen in figure 6.8 for the MSL.

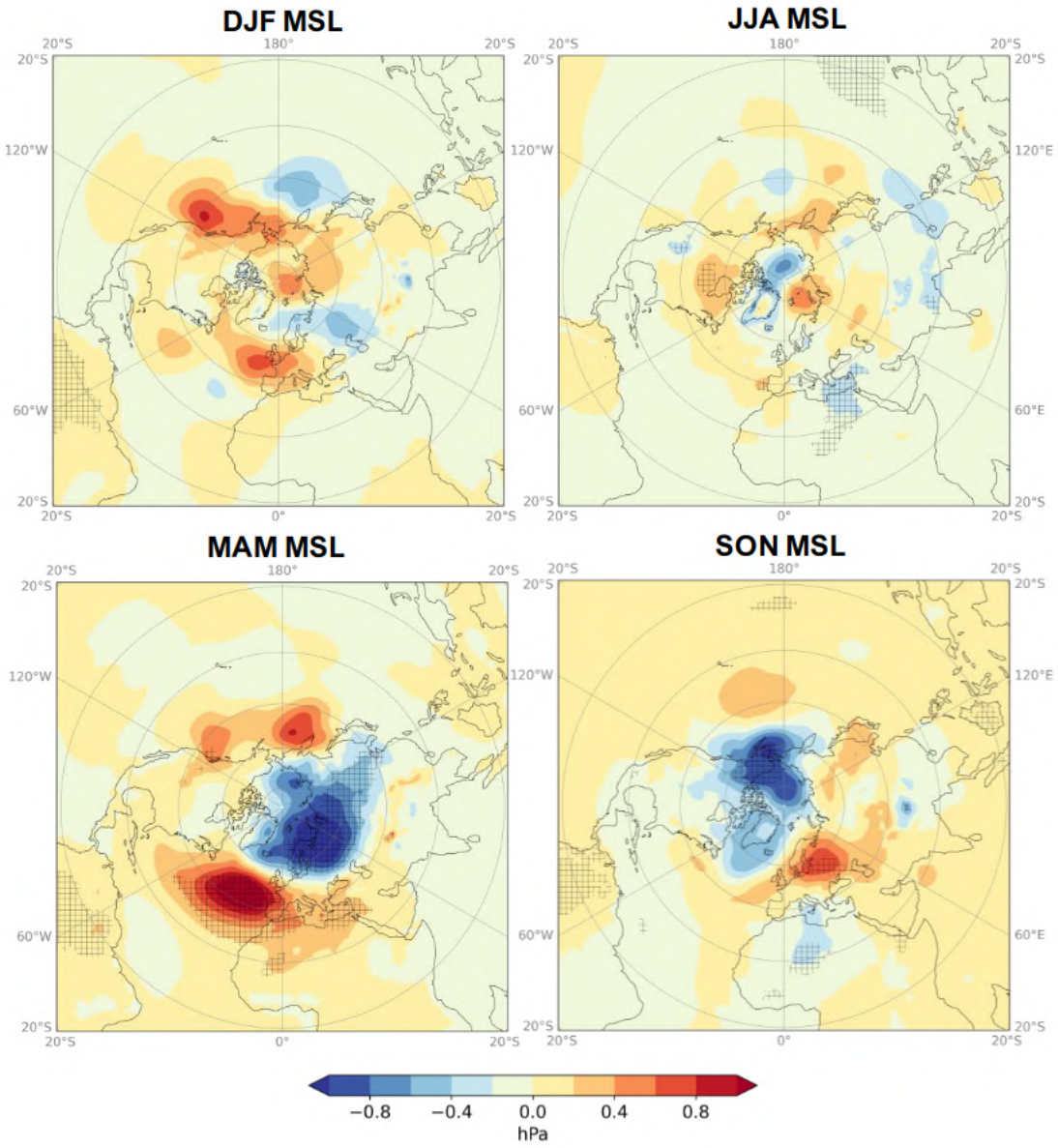

Figure 6.8: The response of the MSL seasonally averaged over the years 1979-2018 (All-LANDICE - All -CTRL). The hatching indicates regions of statistical significance (at significance level $\alpha = 0.05$). An increase in MSL is associated with colder surface temperatures. Anomaly pattern over NH shows 0.2% significant difference in DJF, 13.3 % in MAM, 2.4% in JJA and 4.5% in SON.

The main goal of studying other variables is to see if the new parameterization has potential impacts which were not seen in the temperature comparison or make the hypothesis more robust, i.e., that the internal variability too large to see a systematic response form the albedo parameterization.

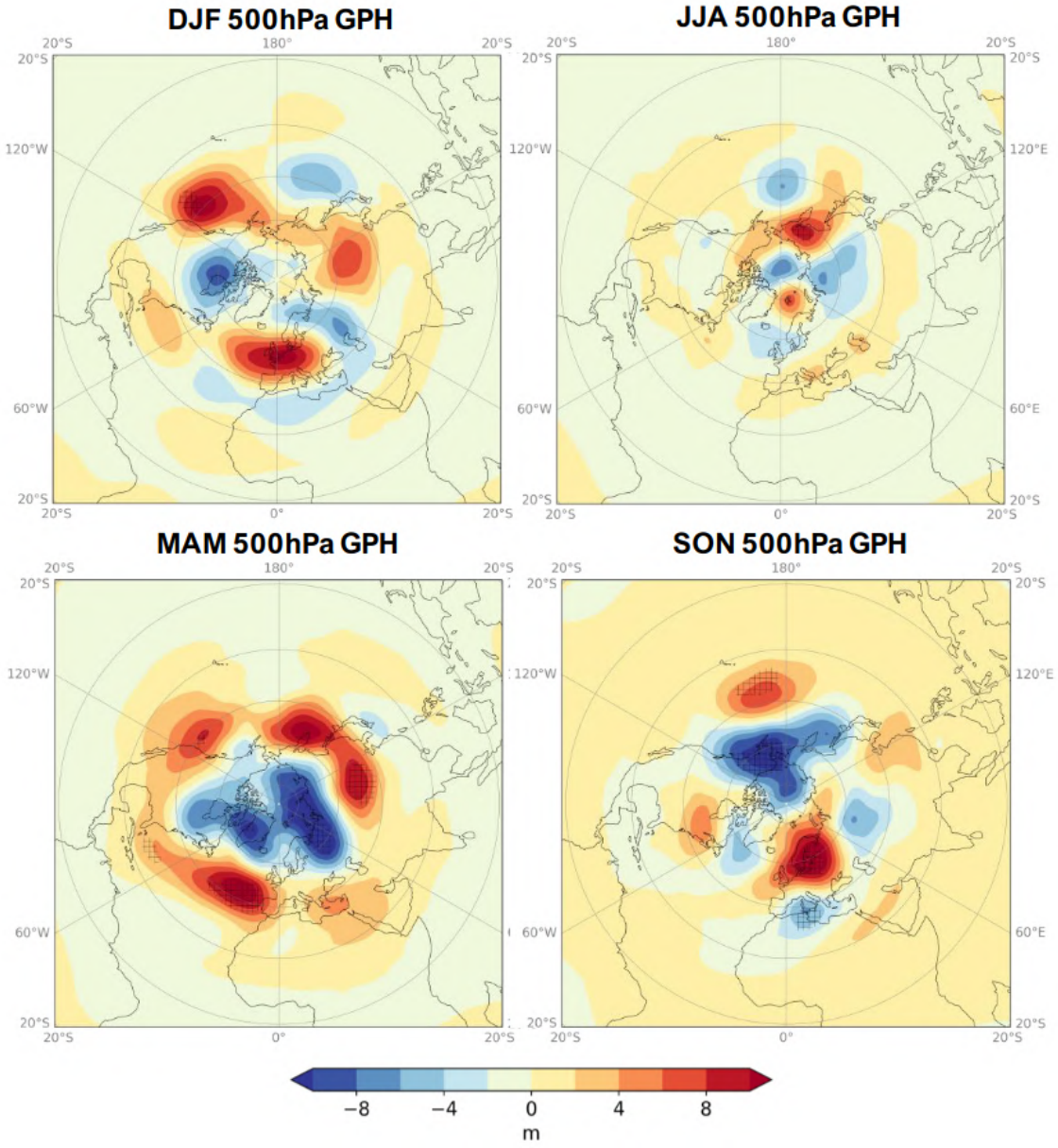

Figure 6.9: The response of the MSL seasonally averaged over the years 1979-2018 (All-LANDICE - All -CTRL). The hatching indicates regions of statistical significance (at significance level $\alpha = 0.05$). An increase in MSL is associated with colder surface temperatures.

To begin with, it is worth noting that the results in figure 6.8 only show little significant difference between the simulations in winter and summer. The most significant response in MSL can be seen in the spring and autumn season. The spring season exhibits a significant strengthening of 1 hPa of the Azores high and the Icelandic

low. In the fall season, a significant lowering of MSL is seen over Alaska. Similar observations can be done for the 500hPa GPH, which is the height of this pressure surface above mean sea level. Here, the response shows significant differences during spring and fall too.

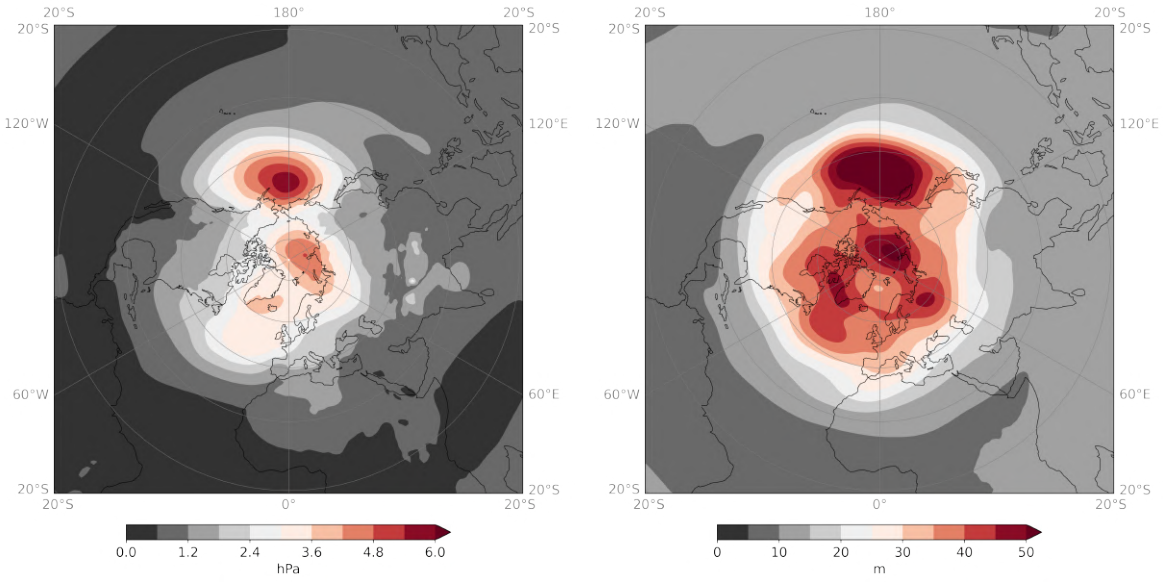

(a) MAM MSL **(b)** MAM 500hPa GPH

Figure 6.10: The 40 year standard deviation in springtime over the All-CTRL ensem- ble between 1979-2018.

This spring pattern could be associated with a positive phase of the Arctic Oscillation (AO). The AO, also known as Northern Annular Mode (NAM), is characterized by a shifting of atmospheric pressure between the Arctic and NH mid latitudes of the North Atlantic and North Pacific. Positive phases of the AO are linked with a northward shift of the storm track and in increased strength of the polar night jet (strong westerly winds around the polar vortex) (Baldwin and Dunkerton, 1999). Moreover, colder T2M around Greenland and warmer T2M over Canada and Siberia. Interestingly, a decrease of T2M around Greenland and the increase over Siberia can be seen in the seasonal temperature comparison for the spring time (see figure 6.6).

Comparing this spring anomaly to the MAM standard deviation of the CTRL runs, we see that anomaly pattern amounts to one third of the standard deviation, as shown in figure 6.10. Moreover, the pattern only shows significant differences at medium variability of the CTRL simulations. Similarly, when looking at the MAM zonal-mean zonal wind (figure A.5), a significant anomaly of about one third of the standard deviation can be seen for the polar night jet. Throughout the other seasons, there are no significant changes in the zonal-mean zonal wind over the northern hemisphere.

As previously discussed the applied forcing is small, so examining the MSL anomaly pattern of a stronger forcing might give an insight if the pattern can be induced by albedo changes. When looking at the All-EXTRM ensemble in reference to the All-CTRL (see figure A.4), significant differences are mainly seen in spring and summer. The spring season shows a similar but weaker negative anomaly pattern over northern Europe and Siberia compared to the LANDICE perturbation. However, the AO pattern is not visible. The strongest response to the extreme forcing is seen in Summer with a large decrease in MSL over the GrIS and similar positive anomaly over the Arctic.

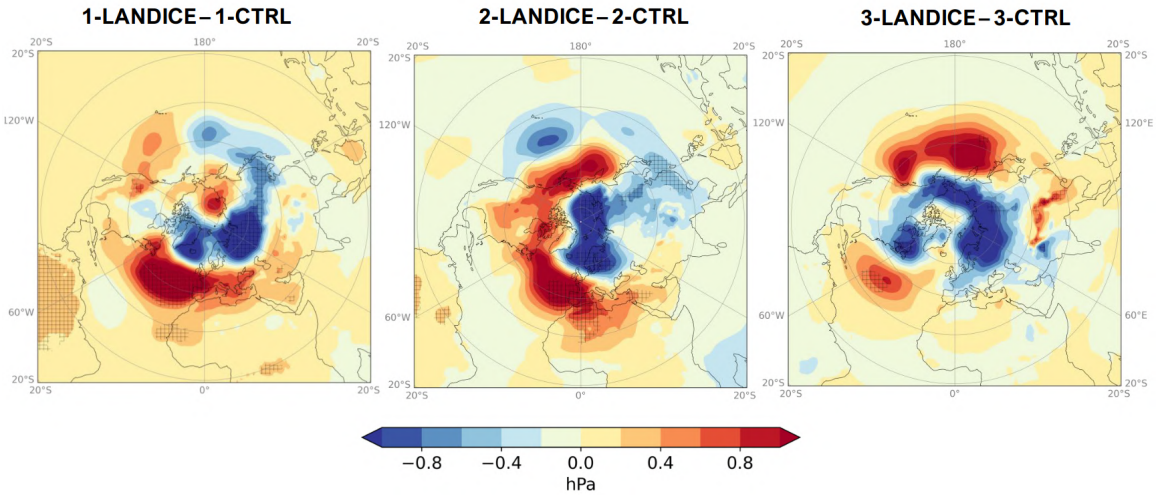

Figure 6.11: Comparison of the MAM difference in the CTRL runs. Hatching indicates significance at 95% level.Anomaly pattern over NH shows 8.5 % for first member, 7.2 % for the second and 2.3% for the third.

Looking at the individual members for the MSL MAM response (fig. 6.11), it can be seen hat the pattern varies in position and is only significant in 2 out of 3 members. The same holds for the 500hPa GPH, which is not shown here. Moreover, an additional comparison of the CTRL runs in MAM season shows again, that differences between the CTRL simulations are large and show strong significant signals over the NH.

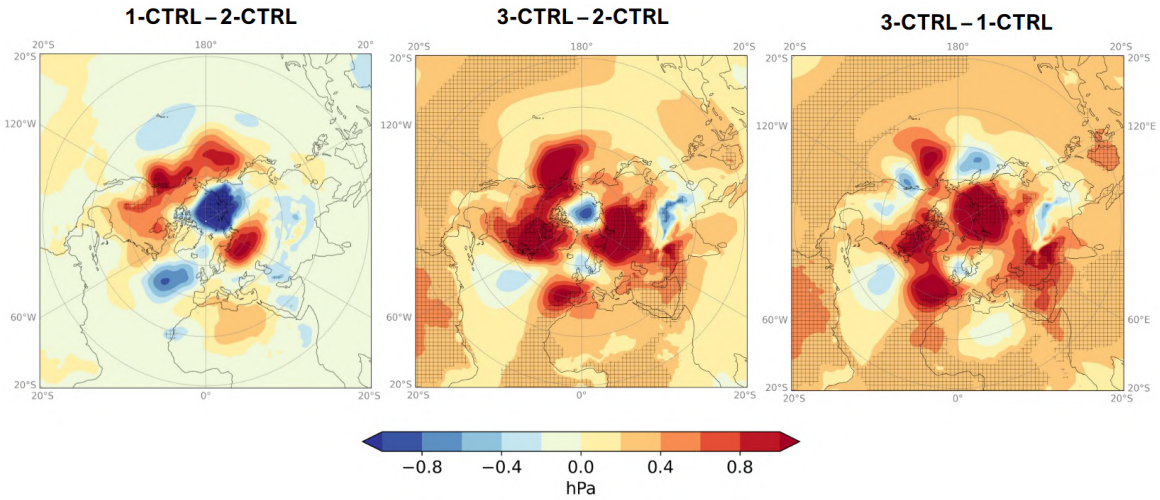

Figure 6.12: Comparison of the MAM difference in the CTRL runs. Hatching indicates significance at 95% level. Anomaly pattern over NH shows 2.58 % for 1-CTRL – 2-CTRL, 23.1% for 3-CTRL – 2-CTRL and 26.3% for 3-CTRL – 1-CTRL.

Summarizing the findings, it can be seen that the response in MSL and 500hPa GPH shows wave train like anomaly patterns, which show statistical significance during the spring and fall. For the spring season only two members show a significant pattern which resembles a positive AO mode. The comparison of the extreme simulation shows no comparable response to the one of LANDICE emsemble. Further, the anomalies amount to one third of the standard deviation.

It should be noted that the scale on which the changes are plotted is to highlight the anomalies, which might give the misleading conclusion that the anomalies a large and thereby significant. As the applied forcing is small, it can be concluded that the observed seasonal anomaly pattern like the AO are not necessarily a forced response, but can arise through the natural variability of the atmosphere.

Chapter 7

Conclusion

In this thesis the atmospheric module of the global climate model EC-Earth3 was used to study the impact of the recently revised snow albedo parameterization on the simulated climate of EC-Earth3. To examine the local and remote climate response an ensemble of three experiments was used – a control experiment, a LANDICE experiment using the new albedo scheme and an extreme experiment with very low albedo of 0.6. Each experiment consists of three members amounting to a total of nine simulations.

The comparison of the simulated albedo to the MODIS satellite observations over Greenland and Ellesmere Island shows that the new albedo parameterization is more responsive to changes in temperature and precipitation. This is advantageous to the previously constant albedo over perennial snow, especially for representing the snow albedo feedback in a warming climate. The new scheme introduces a seasonal evolution of albedo, which overall lowers the albedo over annual averages. Over the northern dry areas of the GrIS the snow albedo is underestimated, highlighting the need for an adjustment of the dry ageing time scale. However, further investigation is needed to better pinpoint the processes affected the albedo and make future adjustments.

The introduced changes in surface radiative and turbulent fluxes, showed that the applied forcing was small, but the lowered albedo lead to an overall increase in energy uptake by the surface of Greenland. As expected, the albedo forcing is stronger with more available insolation, showing its largest impact during summertime.

The aim of this thesis was to see if there is any systematic response linked to the new albedo parameterization. Locally, the new albedo parameterization leads to a more realistic representation of the GrIS, which would reduce EC-Earth3's temperature

biases over the perennial snow and in the ablation zone. However, the remote anomaly pattern found in the annual near surface temperature response was not robust, as it was only produced by two of the three members. Moreover the T2M pattern could be created with similar strength and significance without the new albedo scheme, i.e., by the control runs. Therefore, it can be concluded that the observed pattern is not necessary a forced response but can be explained by the large internal variability of the atmosphere. Consistent with other studies, the large internal variability makes it difficult to see robust responses of small perturbation, especially with only using three members. Therefore, large ensembles wit much more members are needed to thoroughly observe the response.

Similar conclusion can be drawn from looking at the response in mean sea level pressure and 500 hPa geopotential height. The spring anomaly pattern resembles a significant positive phase of the Arctic oscillation, which is only significant in two members and varies spatially in between them. The extreme perturbation shows no comparable pattern, while the comparison of the control simulation shows strong and significant differences. As the significance as well as the amplitude of the identified differences is low, it is concluded that the observed pattern is again attributed to the internal processes of the atmosphere.

Overall, the remote response of the new albedo parameterization shows no systematic pattern. However, the new scheme improves the simulated climate locally. This study highlights the importance of thoroughly analyzing patterns for significance and robustness. Just because a statistical significant anomaly is visible, doesn't necessarily mean it is a forced response. Moreover, the study emphasizes the importance on raising the awareness of internal variability when investigation atmospheric responses to forcings that are of moderate strength.

Appendix A

Additional figures

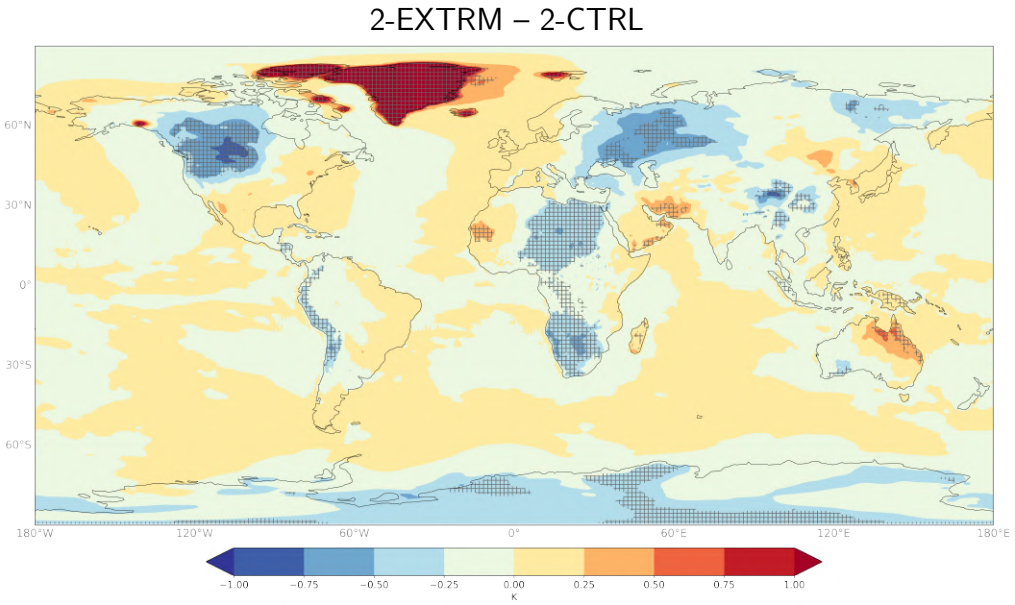

Figure A.1: The difference in annual mean T2M (2-EXTRM - 2-CTRL) for 1979-2018. Hatching indicates significance at 95% significance level. Anomaly pattern shows a 6.6 % significant difference.

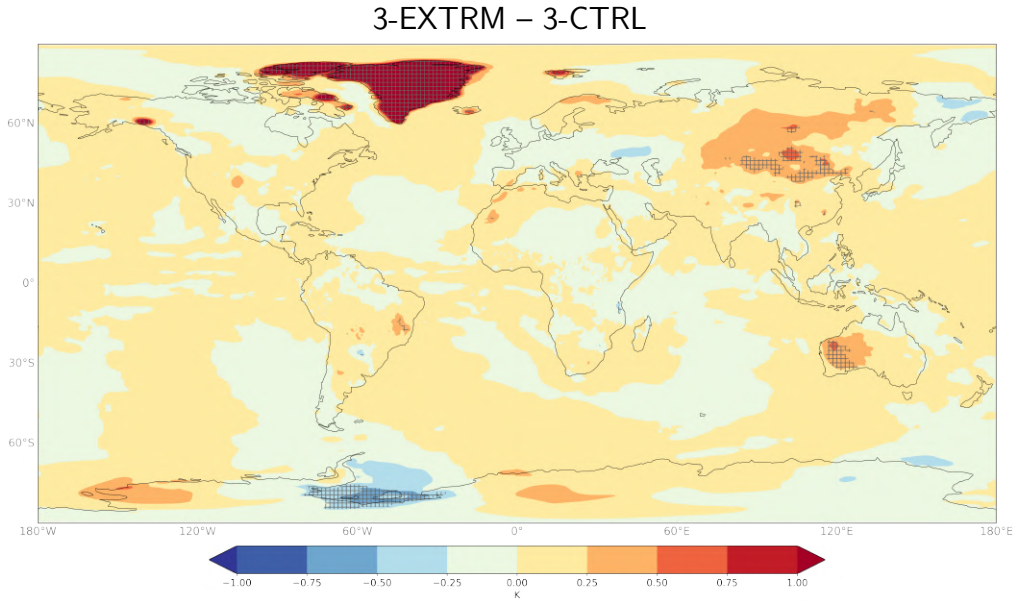

Figure A.2: The difference in annual mean T2M (3-EXTRM - 3-CTRL) for 1979-2018. Hatching indicates significance at 95% significance level. Anomaly pattern shows a 1.4% significant difference.

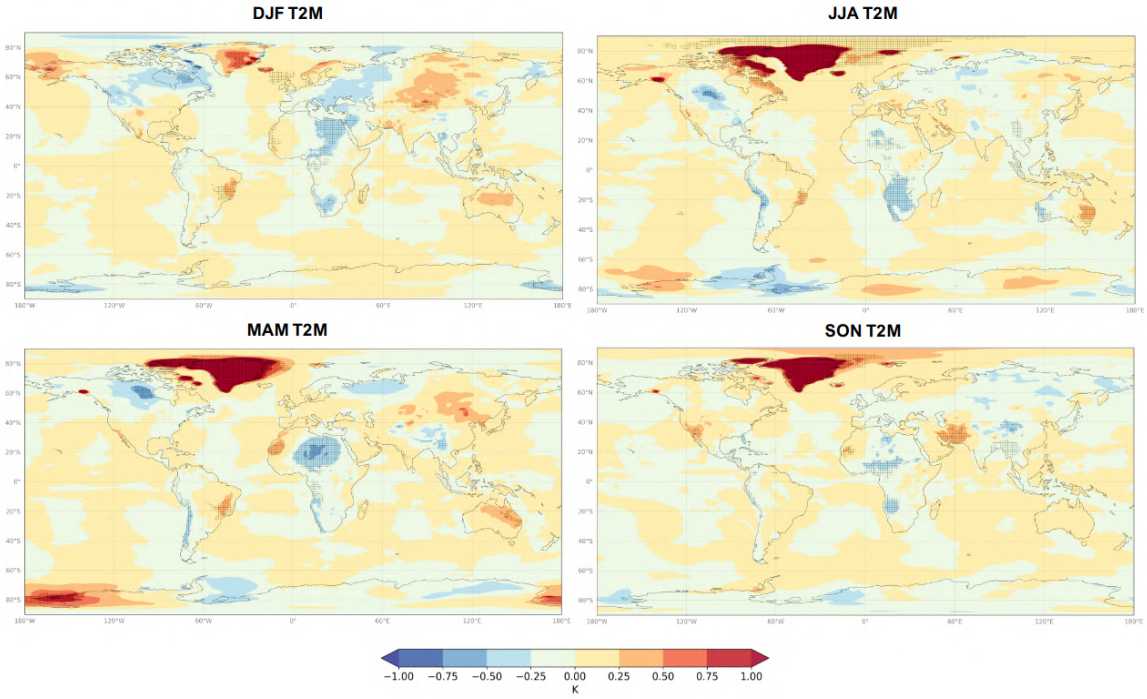

Figure A.3: The difference in seasonal mean T2M (All-EXTRM- All-CTRL) for 1979-2018. Hatching indicates significance at 95% significance level. Anomaly pattern shows a 3.4% significant difference in DJF, 4.6 % in MAM, 5.8% in JJA and 3.9% in SON.

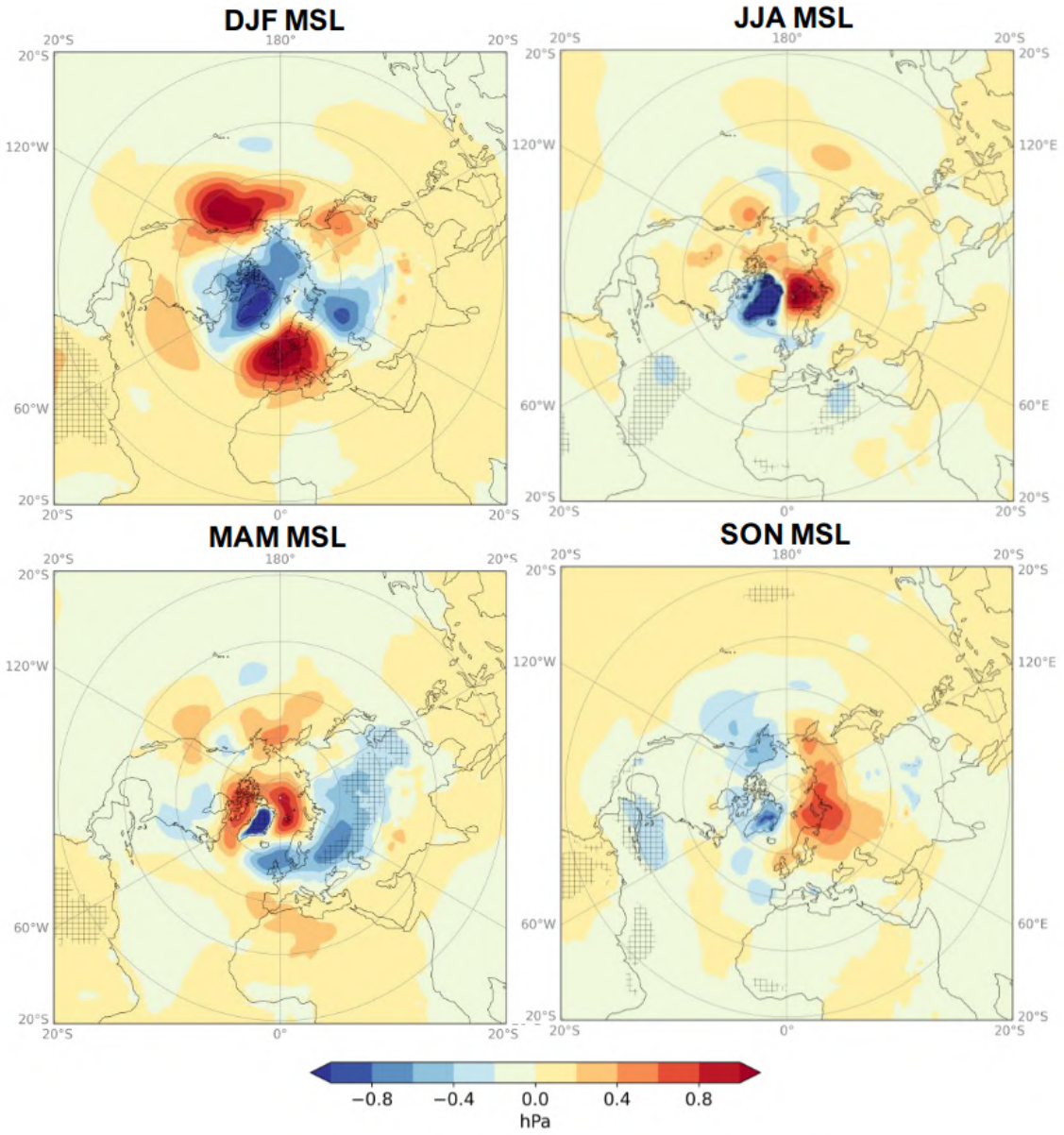

Figure A.4: The difference in seasonal mean MSL (All-EXTRM- All-CTRL) for 1979-2018. Hatching indicates significance at 95% significance level. Anomaly pattern shows a 1.6% significant difference in DJF, 6.11 % in MAM, 5.0% in JJA and 3.4% in SON.

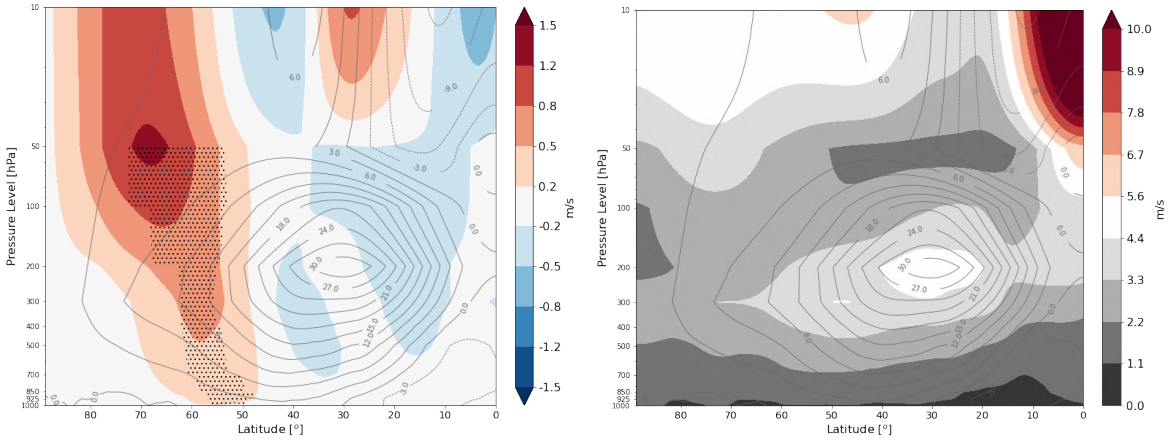

(a) **(b)**

Figure A.5: The zonal mean wind in spring season between All-LANDICE and ALl.CTRL. Hatching indicates significance at 95% level. Background contours show the spring season mean of All-CTRL.

References

Abe-Ouchi, A., Saito, F., Kageyama, M., Braconnot, P., Harrison, S. P., Lambeck, K., Otto-Bliesner, B. L., Peltier, W. R., Tarasov, L., Peterschmitt, J.-Y., and Takahashi, K. (2015). Ice-sheet configuration in the cmip5/pmip3 last glacial maximum experiments. *Geoscientific Model Development*, 8(11):3621–3637.

Ahrens, C. D. and Henson, R. (2017). *Meteorology today: An introduction to weather, climate and the environment*. Cengage Learning, Inc., 12 edition.

Aoki, T., Hachikubo, A., and Hori, M. (2003). Effects of snow physical parameters on shortwave broadband albedos. *Journal of Geophysical Research: Atmospheres*, 108(D19).

Baker, D. G., Ruschy, D. L., and Wall, D. B. (1990). The albedo decay of prairie snows. *Journal of Applied Meteorology and Climatology*, 29(2):179 – 187.

Baldwin, M. P. and Dunkerton, T. J. (1999). Propagation of the arctic oscillation from the stratosphere to the troposphere. *Journal of Geophysical Research: Atmospheres*, 104(D24):30937–30946.

Balsamo, G., Beljaars, A., Scipal, K., Viterbo, P., van den Hurk, B., Hirschi, M., and Betts, A. K. (2009). A revised hydrology for the ecmwf model: Verification from field site to terrestrial water storage and impact in the integrated forecast system. *Journal of Hydrometeorology*, 10(3):623 – 643.

Block, K. and Mauritsen, T. (2013). Forcing and feedback in the mpi-esm-lr coupled model under abruptly quadrupled co2. *Journal of Advances in Modeling Earth Systems*, 5.

Box, J. E., van As, D., and Steffen, K. (2017). Greenland, canadian and icelandic land-ice albedo grids (2000–2016). *GEUS Bulletin*, 38:53–56.

Broccoli, A. and Manabe, S. (1987). The influence of continental ice, atmospheric co2, and land albedo on the climate of the last glacial maximum. *Climate Dynamics*, 1:87–99.

Budyko, M. I. (1969). The effect of solar radiation variations on the climate of the earth. *Tellus*, 21(5):611–619.

Cao, Y., Liang, S., Chen, X., and He, T. (2015). Assessment of sea ice albedo radiative forcing and feedback over the northern hemisphere from 1982 to 2009 using satellite and reanalysis data. *Journal of Climate*, 28(3):1248 – 1259.

Coakley, J. A. (2003). Reflectance and albedo, surface. In Holton, J. R. and Curry, J. A., editors, *Encyclopedia of the Atmosphere*, pages 1914 –1923. Academic Press.

Döscher, R., Acosta, M., Alessandri, A., Anthoni, P., Arsouze, T., Bergman, T., Bernardello, R., Boussetta, S., Caron, L.-P., Carver, G., Castrillo, M., Catalano, F., Cvijanovic, I., Davini, P., Dekker, E., Doblas-Reyes, F. J., Docquier, D., Echevarria, P., Fladrich, U., Fuentes-Franco, R., Gröger, M., v. Hardenberg, J., Hieronymus, J., Karami, M. P., Keskinen, J.-P., Koenigk, T., Makkonen, R., Massonnet, F., Ménégoz, M., Miller, P. A., Moreno-Chamarro, E., Nieradzik, L., van Noije, T., Nolan, P., O'Donnell, D., Ollinaho, P., van den Oord, G., Ortega, P., Prims, O. T., Ramos, A., Reerink, T., Rousset, C., Ruprich-Robert, Y., Le Sager, P., Schmith, T., Schrödner, R., Serva, F., Sicardi, V., Sloth Madsen, M., Smith, B., Tian, T., Tourigny, E., Uotila, P., Vancoppenolle, M., Wang, S., Wårlind, D., Willén, U., Wyser, K., Yang, S., Yepes-Arbós, X., and Zhang, Q. (2022). The ec-earth3 earth system model for the coupled model intercomparison project 6. *Geoscientific Model Development*, 15(7):2973–3020.

Dutra, E., Balsamo, G., Viterbo, P., Miranda, P. M. A., Beljaars, A., Schar, C., and Elder, K. (2010). An improved snow scheme for the ecmwf land surface model: Description and offline validation. (11):899–916.

EC-Earth Consortium (2022). The EC-Earth Consortium. `http://www.ec-earth.org`. Accessed: 2022-03-28.

ECMWF (2021). Part iv: Physical processes. In *IFS DOCUMENTATION – Cy47r3*.

Goosse, H., Kay, J., Armour, K., Bodas-Salcedo, A., Chepfer, H., Docquier, D., Jonko, A., Kushner, P., Lecomte, O., Massonnet, F., Park, H.-S., Pithan, F., Svensson, G., and Vancoppenolle, M. (2018). Quantifying climate feedbacks in polar regions. *Nature Communications*, 9.

Groisman, P., Karl, T., Knight, R., and Stenchikov, G. (1994). Changes of snow cover, temperature, and radiative heat balance over the northern hemisphere. *Journal of Climate*, 7.

Gurvan, M., Bourdallé-Badie, R., Chanut, J., Clementi, E., Coward, A., Ethé, C., Iovino, D., Lea, D., Lévy, C., Lovato, T., Martin, N., Masson, S., Mocavero, S.,

Rousset, C., Storkey, D., Müeller, S., Nurser, G., Bell, M., Samson, G., Mathiot, P., Mele, F., and Moulin, A. (2022). Nemo ocean engine.

Hall, A. (2004). The role of surface albedo feedback in climate. *Journal of Climate*, 17(7):1550 – 1568.

Hartmann, D., Klein Tank, A., Rusticucci, M., Alexander, L., Brönnimann, S., Charabi, Y., Dentener, F., Dlugokencky, E., Easterling, D., Kaplan, A., Soden, B., Thorne, P., Wild, M., and Zhai, P. (2013). Observations: Atmosphere and surface. In Stocker, T., Qin, D., Plattner, G.-K., Tignor, M., Allen, S., Boschung, J., Nauels, A., Xia, Y., Bex, V., and Midgley, P., editors, *Climate Change 2013: The Physical Science Basis. Contribution of Working Group I to the Fifth Assessment Report of the Intergovernmental Panel on Climate Change*, page 159–254, Cambridge, United Kingdom and New York, NY, USA. Cambridge University Press.

Helsen, M. M., van de Wal, R. S. W., Reerink, T. J., Bintanja, R., Madsen, M. S., Yang, S., Li, Q., and Zhang, Q. (2017). On the importance of the albedo parameterization for the mass balance of the greenland ice sheet in ec-earth. *The Cryosphere*, 11(4):1949–1965.

IPCC (2021). Climate change 2021: The physical science basis. contribution of working group i to the sixth assessment report of the intergovernmental panel on climate change [masson-delmotte, v., p. zhai, a. pirani, s.l. connors, c. péan, s. berger, n. caud, y. chen, l. goldfarb, m.i. gomis, m. huang, k. leitzell, e. lonnoy, j.b.r. matthews, t.k. maycock, t. waterfield, o. yelekçi, r. yu, and b. zhou (eds.)]. *Cambridge University Press. In press.*

Kashiwase, H., Ohshima, K. I., Nihashi, S., and Eicken, H. (2017). Evidence for ice-ocean albedo feedback in the arctic ocean shifting to a seasonal ice zone. *Scientific Reportse*, 7:2045–2322.

Køltzow, M. (2007). The effect of a new snow and sea ice albedo scheme on regional climate model simulations. *Journal of Geophysical Research*, 112.

Landrum, L., Holland, M. M., Schneider, D. P., and Hunke, E. (2012). Antarctic sea ice climatology, variability, and late twentieth-century change in ccsm4. *Journal of Climate*, 25(14):4817 – 4838.

Langlois, A., Royer, A., Montpetit, B., Roy, A., and Durocher, M. (2020). Presenting snow grain size and shape distributions in northern canada using a new photographic device allowing 2d and 3d representation of snow grains. *Frontiers in Earth Science*, 7:347.

Li, Y., Wang, T., Zeng, Z., Peng, S., Lian, X., and Piao, S. (2016). Evaluating biases in simulated land surface albedo from cmip5 global climate models. *Journal of Geophysical Research: Atmospheres*, 121(11):6178–6190.

Loeb, N. G., Doelling, D. R., Wang, H., Su, W., Nguyen, C., Corbett, J. G., Liang, L., Mitrescu, C., Rose, F. G., and Kato, S. (2018). Clouds and the earthâ€™s radiant energy system (ceres) energy balanced and filled (ebaf) top-of-atmosphere (toa) edition-4.0 data product. *Journal of Climate*, 31(2):895 – 918.

Lüdemann, D. (2021). Project outside course scope: Sensitivity of climate due to ice and snow albedo. unpublished.

Madsen, M. S., Rodehacke, C., Lindpointner, L., Olesen, M., and Yang, S. (2021). Dmi report 21-17 including a dynamic greenland ice sheet in the ec-earth global climate model. `https://www.dmi.dk/fileadmin/Rapporter/2021/DMI_Report_21-17_Including_a_dynamic_Greenland_Ice_Sheet_in_the_EC-Earth_global_climate_model.pdf`.

Meredith, M., Sommerkorn, M., Cassotta, S., Derksen, C., Ekaykin, A., Hollowed, A., G. Kofinas, A. M., Melbourne-Thomas, J., Muelbert, M., Ottersen, G., Pritchard, H., and Schuur, E. (2019). Polar regions. in: Ipcc special report on the ocean and cryosphere in a changing climate [h.-o. portner, d.c. roberts, v. masson-delmotte, p. zhai, m. tignor, e. poloczanska, k. mintenbeck, a. alegria, m. nicolai, a. okem, j. petzold, b. rama, n.m. weyer (eds.). *Cambridge University Press. In press.*

Miller, L. H. (1956). Table of percentage points of kolmogorov statistics. *Journal of the American Statistical Association*, 51(273):111–121.

North, G. (1975). Theory of energy-balance climate models. *Journal of Atmospheric Sciences*, 32:2033–2043.

Ogawa, F., Keenlyside, N., Gao, Y., Koenigk, T., Yang, S., Suo, L., Wang, T., Gastineau, G., Nakamura, T., Cheung, H. N., Omrani, N.-E., Ukita, J., and Semenov, V. (2018). Evaluating impacts of recent arctic sea ice loss on the northern hemisphere winter climate change. *Geophysical Research Letters*, 45(7):3255–3263.

Oke, T. R. (1987). *Boundary layer climates*. Routledge, 2 edition.

Press, W. H., Flannery, B. P., Teukolsky, S. A., and Vetterling, W. T. (1992). *Numerical Recipes in FORTRAN 77: The Art of Scientific Computing*. Cambridge University Press, 2 edition.

Qu, X. and Hall, A. (2005). Surface contribution to planetary albedo variability in cryosphere regions. *Journal of Climate - J CLIMATE*, 18:5239–5252.

Randall, D. (2015). *An Introduction to the Global Circulation of the Atmosphere*. Princeton University Press.

Rousset, C., Vancoppenolle, M., Madec, G., Fichefet, T., Flavoni, S., Barthélemy, A., Benshila, R., Chanut, J., Levy, C., Masson, S., and Vivier, F. (2015). The louvain-la-neuve sea ice model lim3.6: global and regional capabilities. *Geoscientific Model Development*, 8(10):2991–3005.

Steel, R., Torrie, J., and Dickey, D. (1997). *Principles and Procedures of Statistics: A Biometrical Approach*. McGraw-Hill series in probability and statistics. McGraw-Hill.

Stephens, G. L., O'Brien, D., Webster, P. J., Pilewski, P., Kato, S., and Li, J.-l. (2015). The albedo of earth. *Reviews of Geophysics*, 53(1):141–163.

Storch, H. v. and Zwiers, F. W. (1999). *Statistical Analysis in Climate Research*. Cambridge University Press.

StratusDeck (2021). Vertical temperature structure of the atmosphere.

Tebaldi, C., Arblaster, J. M., and Knutti, R. (2011). Mapping model agreement on future climate projections. *Geophysical Research Letters*, 38(23).

Thackeray, C. W. and Fletcher, C. G. (2016). Snow albedo feedback: Current knowledge, importance, outstanding issues and future directions. *Progress in Physical Geography: Earth and Environment*, 40(3):392–408.

Wallace, J. and Hobbs, P. (2006). *Atmospheric Science: An Introductory Survey*. International Geophysics. Elsevier Science.

Wang, X. and Zender, C. S. (2011). Arctic and antarctic diurnal and seasonal variations of snow albedo from multiyear baseline surface radiation network measurements. *Journal of Geophysical Research: Earth Surface*, 116(F3).

Wiscombe, W. and Warren, S. (1980). A model for the spectral albedo of snow. i: Pure snow. *Journal of The Atmospheric Sciences - J ATMOS SCI*, 37:2712–2733.

Xiao, L., Che, T., Chen, L., Xie, H., and Dai, L. (2017). Quantifying snow albedo radiative forcing and its feedback during 2003–2016. *Remote Sensing*, 9(9).

Zunz, V., Goosse, H., and Massonnet, F. (2013). How does internal variability influence the ability of cmip5 models to reproduce the recent trend in southern ocean sea ice extent? *The Cryosphere*, 7(2):451–468.